

AD-757 075

LASER-DOPPLER ANEMOMETER MEASUREMENTS  
OF TURBULENCE IN DRAG REDUCING FLOWS

Gordon L. Guenterberg

Michigan University

Prepared for:

Office of Naval Research

December 1972

DISTRIBUTED BY:

**NTIS**

National Technical Information Service  
U. S. DEPARTMENT OF COMMERCE  
5285 Port Royal Road, Springfield Va. 22151

The University of Michigan  
College of Engineering  
Department of Engineering Mechanics

Technical Report

LASER-DOPPLER ANEMOMETER MEASUREMENTS  
OF TURBULENCE IN DRAG REDUCING FLOWS

by  
Gordon Lee Guenterberg

William P. Graebel, Project Director

ORA Project 065050

Under Contract with:

Department of the Navy

Office of Naval Research

Contract No. N00014-67-A-0181-0030

Arlington, Virginia

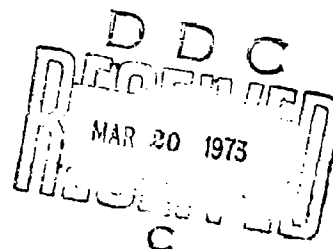
Administered through

Office of Research Administration, Ann Arbor

December 1972

Distribution of this document is unlimited

Reproduced by  
NATIONAL TECHNICAL  
INFORMATION SERVICE  
U S Department of Commerce  
Springfield VA 22151



UNCLASSIFIED

Security Classification

DOCUMENT CONTROL DATA - R&D		
(Security classification of title, body of abstract and indexing annotation must be entered when the overall report is classified)		
1. ORIGINATING AGENCY (Corporate author) The University of Michigan Department of Engineering Mechanics Ann Arbor, Michigan		2a. REPORT SECURITY CLASSIFICATION Unclassified
		2b. GROUP
3. REPORT TITLE Laser-Doppler Anemometer Measurements of Turbulence in Drag Reducing Flows		
4. DESCRIPTIVE NOTES (Type of report and inclusive dates) Project Report		
5. AUTHOR(S) (Last name, first name, initial) Gordon L. Guenterberg		
6. REPORT DATE December 1972	7a. TOTAL NO. OF PAGES 100/01	7b. NO. OF REFS 04
8a. CONTRACT OR GRANT NO. N00014-67-A-0181-0030	9a. ORIGINATOR'S REPORT NUMBER(S) ---	
b. PROJECT NO.		
c.	9b. OTHER REPORT NO(S) (Any other numbers that may be assigned this report) ---	
d.		
10. AVAILABILITY/LIMITATION NOTICES Distribution of this document is unlimited		
11. SUPPLEMENTARY NOTES Details of illustrations in this document may be better studied on microfiche.		12. SPONSORING MILITARY ACTIVITY Department of the Navy, Office of Naval Research, Arlington, Virginia
13. ABSTRACT The drag reduction, mean flow, and turbulence properties of several concentrations of Separan AP30 and water in a fully developed turbulent pipe flow were studied using a two-component laser-Doppler anemometer. This measurement technique was chosen because of its inherent advantages over the traditional measuring techniques that have been used in previous studies of drag reducing flows. A single-pass flow system was used in order to minimize polymer degradation. Polystyrene particles manufactured at The University of Michigan were injected into the flow with a piston pump to provide a scattering medium for the laser light. A polymer injection technique was used. A slurry of methanol and polymer powder was injected directly into the flowing water, providing a fresh, unaged polymer solution. Measurements were made of drag reduction, axial mean velocity, axial turbulence intensity, and Reynolds' stress profiles as well as one-dimensional energy spectra for flows of water and 50, 100, and 200 parts per million solutions of Separan AP30 and water. (The energy spectra were taken at $r = 1.00$ , $0.500$ , and $0.020$ , where $r = 1.00$ is the flow axis.) Results of the drag reduction measurements indicate less drag reduction than reported by previous investigators using the same polymer, polymer concentrations, and flow conditions, of due to incompletely dissolved polymer powder.		

DD FORM 1473  
1 JAN 64

UNCLASSIFIED

Security Classification

I

KEY WORDS	LINK A		LINK B		LINK C	
	ROLE	WT	ROLE	WT	ROLE	WT
Drag reduction; Separan AP 30; laser doppler anemometer						

## INSTRUCTIONS

**ORIGINATING ACTIVITY:** Enter the name and address of the contractor, subcontractor, grantee, Department of Defense activity or other organization (*corporate author*) issuing report.

**REPORT SECURITY CLASSIFICATION:** Enter the overall security classification of the report. Indicate whether "Restricted Data" is included. Marking is to be in accordance with appropriate security regulations.

**GROUP:** Automatic downgrading is specified in DoD Directive 5200.10 and Armed Forces Industrial Manual. Enter group number. Also, when applicable, show that optional markings have been used for Group 3 and Group 4 as authorized.

**REPORT TITLE:** Enter the complete report title in all capital letters. Titles in all cases should be unclassified. A meaningful title cannot be selected without classification, show title classification in all capitals in parentheses immediately following the title.

**DESCRIPTIVE NOTES:** 1. appropriate, enter the type of report, e.g., interim, progress, summary, annual, or final. 2. the inclusive dates when a specific reporting period is entered.

**AUTHOR(S):** Enter the name(s) of author(s) as shown on the report. Enter last name, first name, middle initial. Military, show rank and branch of service. The name of principal author is an absolute minimum requirement.

**REPORT DATE:** Enter the date of the report as day, month, year, or month, year. If more than one date appears on the report, use date of publication.

**TOTAL NUMBER OF PAGES:** The total page count should follow normal pagination procedures, i.e., enter the number of pages containing information.

**NUMBER OF REFERENCES:** Enter the total number of references cited in the report.

**CONTRACT OR GRANT NUMBER:** If appropriate, enter applicable number of the contract or grant under which report was written.

**8c, & 8d. PROJECT NUMBER:** Enter the appropriate military department identification, such as project number, project number, system numbers, task number, etc.

**ORIGINATOR'S REPORT NUMBER(S):** Enter the official report number by which the document will be identified controlled by the originating activity. This number must be unique to this report.

**OTHER REPORT NUMBER(S):** If the report has been assigned any other report numbers (either by the originator or the sponsor), also enter this number(s).

**AVAILABILITY/LIMITATION NOTICES:** Enter any limitations on further dissemination of the report, other than those

imposed by security classification, using standard statements such as:

- (1) "Qualified requesters may obtain copies of this report from DDC."
- (2) "Foreign announcement and dissemination of this report by DDC is not authorized."
- (3) "U. S. Government agencies may obtain copies of this report directly from DDC. Other qualified DDC users shall request through \_\_\_\_\_."
- (4) "U. S. military agencies may obtain copies of this report directly from DDC. Other qualified users shall request through \_\_\_\_\_."
- (5) "All distribution of this report is controlled. Qualified DDC users shall request through \_\_\_\_\_."

If the report has been furnished to the Office of Technical Services, Department of Commerce, for sale to the public, indicate this fact and enter the price, if known.

**11. SUPPLEMENTARY NOTES:** Use for additional explanatory notes.

**12. SPONSORING MILITARY ACTIVITY:** Enter the name of the departmental project office or laboratory sponsoring (paying for) the research and development. Include address.

**13. ABSTRACT:** Enter an abstract giving a brief and factual summary of the document indicative of the report, even though it may also appear elsewhere in the body of the technical report. If additional space is required, a continuation sheet shall be attached.

It is highly desirable that the abstract of classified reports be unclassified. Each paragraph of the abstract shall end with an indication of the military security classification of the information in the paragraph, represented as (TS), (S), (C), or (U).

There is no limitation on the length of the abstract. However, the suggested length is from 150 to 225 words.

**14. KEY WORDS:** Key words are technically meaningful terms or short phrases that characterize a report and may be used as index entries for cataloging the report. Key words must be selected so that no security classification is required. Identifiers, such as equipment model designation, trade name, military project code name, geographic location, may be used as key words but will be followed by an indication of technical context. The assignment of links, rules, and weights is optional.

UNCLASSIFIED

Security Classification

II

# TABLE OF CONTENTS

	<u>Page</u>
Acknowledgments	ii
List of Tables	v
List of Figures	vi
List of Appendices	viii
Chapter	
1. Introduction	1
2. The Principle of Operation of the Laser-Doppler Anemometer	9
3. The Optical System	17
1. Optical Arrangement	17
2. Optical Geometry	19
3. Optical Components	20
Signal-to-Noise Considerations for the Laser-Doppler Anemometer	28
1. Noise in the P.M. Tube	29
2. Noise in the Signal	29
3. Optical Loss Coefficients	33
4. Instrumental Broadening	38
5. Flow System	44
1. Description of the Flow System	44
2. Polymer Injection	46
3. Scattering Particles	47
6. Signal Processing	49
1. Readout Unit	49
2. Signal Processing Set-Up	51
3. Signal Processing	52

## TABLE OF CONTENTS (Continued)

	<u>Page</u>
7. Measurement and Observations	59
1. Discussion of the Turbulence Measuring Technique	59
2. Discussion of Results	60
2.1 Drag Reduction	60
2.2 Mean Velocity Profiles	63
2.3 Turbulence Intensities	65
2.4 Reynolds' Stress	68
2.5 Energy Spectra	70
3. Summary and Conclusion	75
References	78
Appendix A	83
Appendix B	87

## LIST OF FIGURES

<u>Figure</u>	<u>Page</u>
2.1      Optical Geometry for a Laser-Doppler Anemometer	10
2.2      Optical Arrangement of Foreman et al	12
2.3      Optical Arrangement of Goldstein and Kreid	13
2.4      Optical Geometry for the Two-Component Laser-Doppler Anemometer	14
3.1      Optical Bench	18
3.2      Transmitting Optics	23
3.3      Receiving Optics	24
4.1      Optical Arrangement of Rudd	37
4.2      Geometry of Aperture Broadening	40
5.1      Flow System	45
6.1      Readout Unit Circuitry	50
6.2      Signal Processing Set-Up	54
7.1      Axial Mean Velocity Profiles at $Re = 5(10)^4$	64
7.2      Axial Turbulence Intensities at $Re = 5(10)^4$	66
7.3      Reynolds' stress at $Re = 5(10)^4$	69
7.4 $V'_z$ Energy Spectra at $\bar{r} = 1.00$ at $Re = 5(10)^4$	71
7.5 $V'_z$ Energy Spectra at $\bar{r} = 0.500$ at $Re = 5(10)^4$	72
7.6 $V'_z$ Energy Spectra at $\bar{r} = 0.020$ Except for Water at $\bar{r} = 0.32$ at $Re = 5(10)^4$	73

## LIST OF TABLES

<u>Table</u>		<u>Page</u>
7.1	Drag Reduction Parameters	62



<u>Figure</u>		<u>Page</u>
A.1	The Refraction of Beams Due to the Presence of the Test Section and Water	84
B.1	Top View of the Test Section Showing the Refraction of the Beam Geometry Used to Measure the Swirl Component of Velocity Due to the Presence of the Test Section and Water	88

## LIST OF APPENDICES

<u>Appendix</u>		<u>Page</u>
A	Refractive Effect of Test Section and Water on Beam Geometry of a Two-Component Laser-Doppler Anemometer	83
B	Measurement Technique for Measuring the Swirl Component of Velocity	87
	1. Frequency-to-Velocity Relationship	87
	2. Measurement of Turbulent Fluctuations About a Zero Mean	89
	3. Refractive Effect of Test Section and Water on Beam Geometry	91

## Chapter I

### INTRODUCTION

The drastic reduction of wall shear stress induced by the addition of small amounts of high molecular weight polymer to a solvent flow was first observed by Toms (1948) twenty-four years ago.

Since then many theories have been proposed to explain the drag reduction phenomenon. Toms (1948) postulated the existence of a shear thinning wall layer of low viscosity, in the polymer flow, which would yield lower friction coefficients than in the solvent flow. However, rheograms of drag reducing polymer solutions obtained by conventional viscometry methods have shown Newtonian rather than shear thinning behavior.

It has also been speculated that the polymer induces an anisotropic viscosity, that is, a viscosity which is low in the direction of flow but high enough in the other directions to dampen turbulent fluctuations. Differences in normal stresses may provide such a mechanism. Gadd (1968) measured normal stresses in several polymer solutions and found, with one exception, that there was no significant difference in the stress components. He concluded, therefore, that there is no correlation between difference in normal stresses and effectiveness in drag reduction.

Lumley (1967) suggested that molecule entanglements extending across the stream resist the formation of the streamwise vortices and therefore enlarge the sublayer eddies. In a similar vein, Peterlin (1970)

sees one end of the polymer macromolecule lying in the core of a "microvortex", the other end lying outside. The macromolecule is thus deformed; while being deformed it absorbs energy and dissipates the vortex.

Walsh (1967) has proposed one of the more interesting and comprehensive theories to date. He begins by assuming that the disturbances responsible for Reynolds' stresses are born at the edge of the sublayer and that the primary role of the random turbulence in the wall shear layer is to excite a violent repetitive instability in the sublayer flow. The breakdown of this instability produces a small disturbance at the edge of the viscous sublayer. This small disturbance tends to grow because it can locally extract energy from the mean velocity profile through momentum transfer. Simultaneously this small disturbance tends to lose energy because its gradients locally dissipate energy into heat and locally store energy in the polymer molecules. If a small disturbance extracts more energy locally than it loses, it will grow. The disturbances, or vortices, so generated move out from the wall as they are convected downstream. These small disturbances ultimately become part of the structure of the turbulence in the wall shear layer and ultimately become responsible for the Reynolds' stresses of turbulent flow.

The idea fundamental to this theory is that large scale disturbances which produce Reynolds' stresses some distances downstream were, at an earlier time, small disturbances at the edge of the viscous sublayer

some distances upstream. Once the small disturbances start to grow, the effect of the polymer molecules may be neglected. All that the polymer molecules do is to slightly alter the energy balance of the turbulence fluctuations close to the wall. By alteration, the molecules allow viscous dissipation to destroy disturbances which would have had sufficient energy to grow had the polymer molecules not been present. By decreasing the number of small disturbances which grow per unit area and time and move out from the edge of the viscous sublayer, the addition of polymer molecules ultimately changes the structure of the turbulence in the wall shear layer. This change results in lower Reynolds' stresses and thus lower turbulent momentum transport.

The experimental investigation of the turbulent structure of drag reducing flows has been the subject of study for many researchers. Rodriguez, Patterson, and Zankin (1971) as well as Wells, Harkness, and Meyer (1968) measured turbulence intensities using piezoelectric probes. Seyer and Metzner (1969) measured mean velocity profiles and the axial and radial turbulence intensities for a drag reducing flow using an air bubble visualization technique. Shaver and Merrill (1959) used a dye injection technique to qualitatively measure the effect of polymer addition on turbulence. Virk et al (1967) and Patterson and Zankin (1967) measured mean velocity profiles and axial intensities with hot film anemometers.

Nicedemo, Acierno, and Astarita (1969) and Elata, Lehrer, and Kahanovitz (1966) measured velocity profiles using Pitot tube probes. More recently Rudd (1972) measured the axial mean velocity profiles and turbulence intensities in a pipe with square cross-section using a laser anemometer technique. Using a similar technique, Chung and Graebel (1972) made these measurements in a pipe with round cross-section, as well as energy spectra at various radial stations.

The results of many of these experiments are inconclusive. Much of the data shows a large degree of scatter. Seyer and Metzner (1969) have observed significant differences in the axial turbulence intensities of the polymer solution as compared to a water flow. However, these differences are of the same order of magnitude as their confidence band. Thus, it is not clear whether these noted differences are real or only apparent.

Many of these experimental results are also questionable due to the measuring techniques used. Astarita and Nicodemo (1966) among others have questioned the accuracy of measurements made using hot film anemometers and Pitot tube probes. Pitot tube errors are attributed to the fact that: (a) the influence of the normal stress is significant; (b) the time average of the fluctuating stresses is not simply related to the time average of the velocity fluctuations; (c) the boundary-layer thickness on the pressure probe may be large compared to the probe size; (d) a large size Pitot tube is needed to minimize calibration errors (Metzner and Astarita, (1967) ).

Hot-film anemometers have different heat transfer characteristics in polymer solutions than in water and therefore cannot be calibrated using the usual heat transfer laws. They further suffer from the problem of a time dependant calibration due to the buildup of polymer molecules near the stagnation region of the probe (Lumley, 1969).

It is not surprising, then, that these investigators report contradictory results. For example, Virk et al (1967) measured higher axial turbulence intensities for the polymer solution across a pipe flow, as compared to solvent flow, whereas Seyer and Metzner (1969) measured lower intensities in the same region of a pipe flow. On the other hand, Wells, Harkness, and Meyer (1968) conclude from their results that the axial turbulence intensity is unchanged for the polymer solution across the pipe cross-section.

Most authors agree that there is some sort of interaction between the polymer molecules and the turbulent eddies such that the turbulent flow structure is altered. It is further generally agreed that the predominant alteration occurs near the solid boundary, that is, in the vicinity of the viscous sublayer. There is, however, little data documenting the turbulence processes close to the wall.

The experimental picture would be bleak indeed, if it were not for the development of the laser-Doppler anemometer. In the laser-Doppler anemometer one projects a beam of laser light through a flow into which minute particles have been injected. These particles serve to scatter the incident light, inducing a Doppler frequency shift in the

scattered light which is proportional to the fluid velocity. Further details of this process will be discussed later. Using this technique, Rudd (1972) has overcome many of the experimental problems inherent in measuring polymer flows and had measured the axial mean velocity and turbulence intensity profiles well into the viscous sublayer. Thus he was able to verify the growth of the laminar sublayer which was predicted by Elata, Lehrer, and Kahanovitz (1966). (The growth of the laminar sublayer in polymer flows was also observed indirectly by Virk (1971a)). This growth is explained to be the consequence of damping of high wave number turbulence by the polymer molecules.

The laser anemometer measuring technique shows a great deal of promise as it has many inherent advantages over traditional fluid flow measuring devices such as hot-wire and hot film anemometers and Pitot tube probes. It is more accurate over a wide range of velocities; its response is linear to any component of velocity independent of other components; its' absolute characteristics, determined by optical configuration and the frequency of the laser light used, eliminate the need for calibration under operating conditions; it has a faster response to turbulent fluctuations; and it offers greater spatial resolution which permits a highly localized probe of velocity without perturbation of the flow (Jackson and Paul, 1971).

Since its first development and use by Yeh and Cummins (1964), the laser-Doppler anemometer (hereafter abbreviated as LDA) has experienced



rapid development. Foreman et al (1965) devised a practical means of detecting the time varying Doppler frequency shift.

Goldstein and Kried (1967) used the LDA to measure flow development. Their optical configuration offers some decided advantages over that of Foreman et al.

Rolfe et al (1968) developed design criteria for the LDA and constructed a LDA capable of measuring turbulence properties of a flow in all three coordinate directions. One outgrowth of Rolfe's work has been the design and manufacture of a wideband frequency tracker by Fridman, Kinnard, and Meister (1969), which, as with Foreman's device, solves the knotty problem of extracting the real-time velocity information from the time varying output of the LDA.

Because of its many advantages and its proven success in overcoming the problems inherent in making measurements in polymer flows, a LDA was used in the present work. Using this technique, turbulence measurements of drag reducing flows were made in a two inch diameter pipe. The goal of the present work was to extend our knowledge of the turbulent structure of drag reducing flows in two ways: first, by documenting turbulence parameters not measured previously, such as the Reynolds' stress, autocorrelation function, radial energy spectra, and the instantaneous product of the velocity fluctuations. (This last measurement was made in order to learn more about the production of turbulent energy.) Secondly, measurements of all the turbulence parameters documented (mean velocity, axial and radial intensities,

Reynolds' stress, energy spectra, the autocorrelation function, and the product of the velocity fluctuations) were made in the region close to the wall. As mentioned previously, most authors feel that the polymer-turbulence interaction that results in drag reduction occurs in this region. It is hoped that the results of these measurements will add new insight into the basic nature of the drag reduction phenomenon.

## Chapter II

### THE PRINCIPLE OF OPERATION OF THE LASER-DOPPLER ANEMOMETER

The principle of operation of a laser-Doppler anemometer can be briefly described as follows: an incident beam of laser light (in the direction designated by the unit vector  $\underline{k}_0$  in Figure 2.1), is focused at point 0 in a fluid stream whose velocity at 0 is  $\underline{V}$ . The incident beam is scattered due to the presence of minute particles injected into the flow. The particles move with nearly the velocity  $\underline{V}$  (Huffaker, 1970). A portion of the scattered front, a beam denoted by  $\underline{k}_s$  in Figure 2.1, has a Doppler-shifted frequency  $f_s = f_0 + f_d$ , where  $f_s$  is the frequency of the scattered light,  $f_0$  is the frequency of the incident light, and  $f_d$  is the Doppler shift due to scattering. The Doppler-shifted frequency,  $f_d$ , is directly proportional to the velocity of the scattering particles at point 0 (the exact relationship is developed below), thus  $f_d$  is a measure of the stream velocity  $\underline{V}$  at point 0. In order to detect  $f_d$ , a reference beam of the initial frequency is aligned so as to coincide with the scattered beam and is focused at point 0. The scattered and reference beams are optically mixed at point 0. The resulting beam is optically heterodyned on the photo cathode surface of a photomultiplier tube to produce a beat signal with a frequency of the Doppler shift,  $f_d$ . Thus the photomultiplier (P.M.) output signal is a voltage whose frequency is the Doppler-shifted frequency.

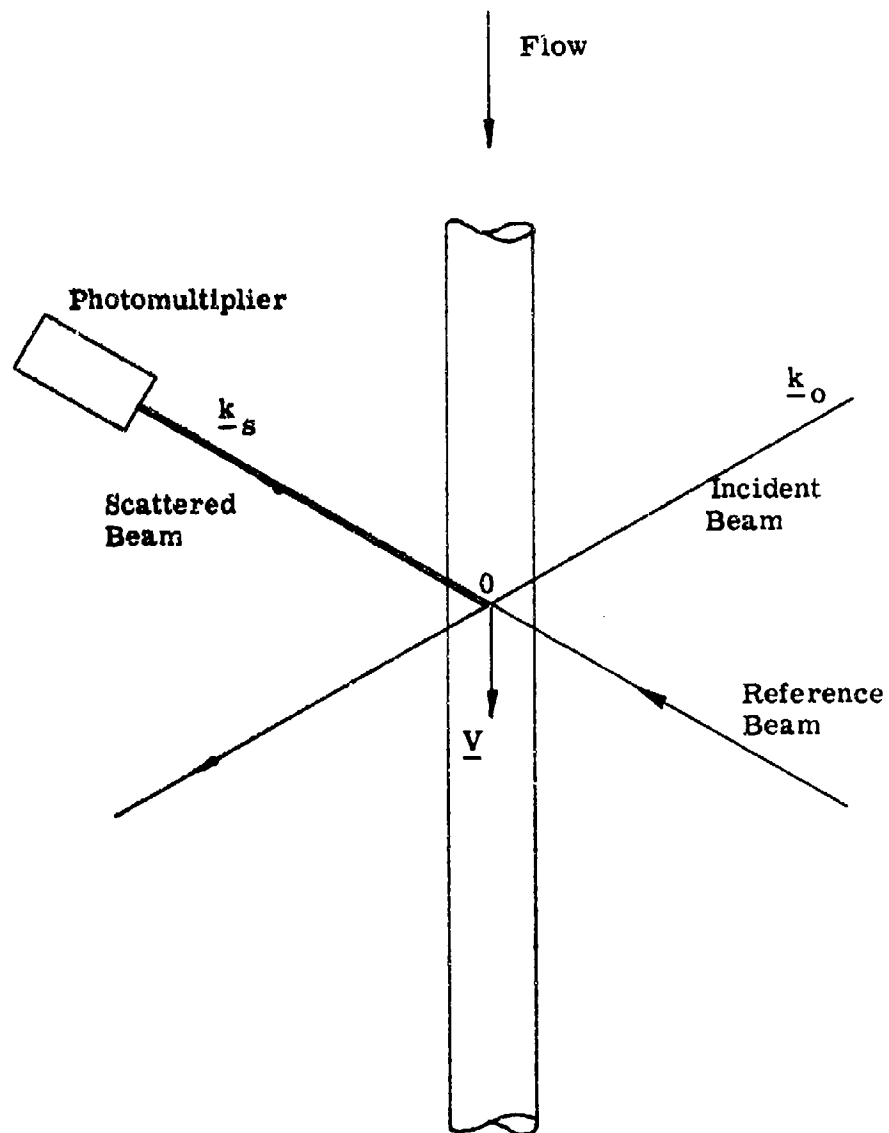


Figure 2.1

Optical Geometry for a Laser-Doppler Anemometer

The relationship between the Doppler frequency shift,  $f_d$ , and the velocity  $\underline{V}$  can be found in the following manner: the incident frequency,  $f'$ , as seen by an observer moving with the flow, is

$$(2.1) \quad f' = f_o \left( 1 - \frac{\underline{V} \cdot \underline{k}_o}{C} \right),$$

where  $C$  is the velocity of light in the fluid, and  $\underline{k}_o$  and  $\underline{k}_s$  are the unit vectors in the direction of the incident and scattered beams respectively.

The frequency  $f_s$  of light scattered by particles moving with the flow and received by a stationary detector, say the P.M., is

$$(2.2) \quad f_s = f' \left( 1 + \frac{\underline{V} \cdot \underline{k}_s}{C} \right).$$

It follows that

$$(2.3) \quad f_s = f_o \left( 1 - \frac{\underline{V} \cdot \underline{k}_o}{C} \right) \left( 1 + \frac{\underline{V} \cdot \underline{k}_s}{C} \right).$$

The Doppler frequency shift,  $f_d$ , then becomes

$$(2.4) \quad f_d = f_o \left[ \frac{\underline{V}}{C} \cdot (\underline{k}_s - \underline{k}_o) - \left( \frac{\underline{V} \cdot \underline{k}_o}{C} \right) \left( \frac{\underline{V} \cdot \underline{k}_s}{C} \right) \right],$$

which to order  $\left| \frac{\underline{V}}{C} \right|$  is

$$(2.5) \quad f_d = \frac{f_o}{C} \underline{V} \cdot (\underline{k}_s - \underline{k}_o).$$

The optical arrangement used by Foreman et al (1965) is shown in Figure 2.2 and that of Goldstein and Kreid (1967) in Figure 2.3. Because of its relation ease of alignment, a two-component variation of Goldstein's arrangement was used in this work (see Figure 3.1).

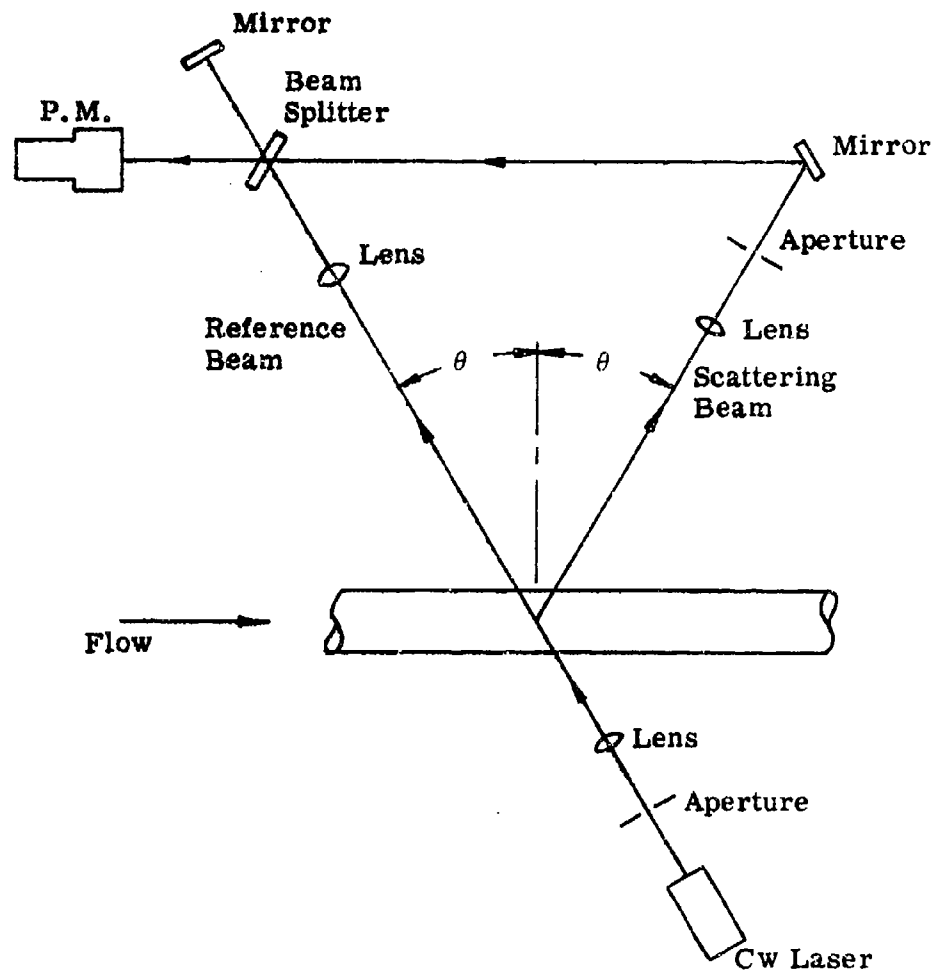


Figure 2. 2

Optical Arrangement of Foreman et al (1966)

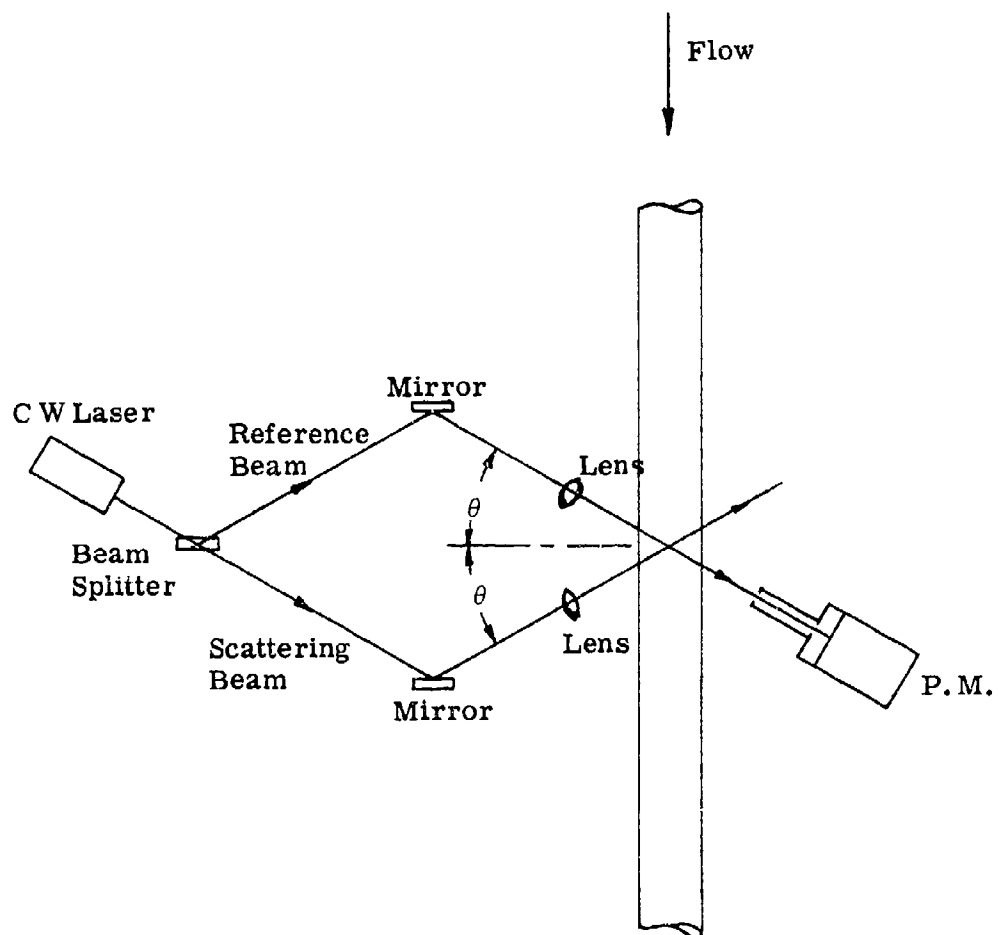


Figure 2.3

Optical Arrangement of Goldstein and Kreid (1967)

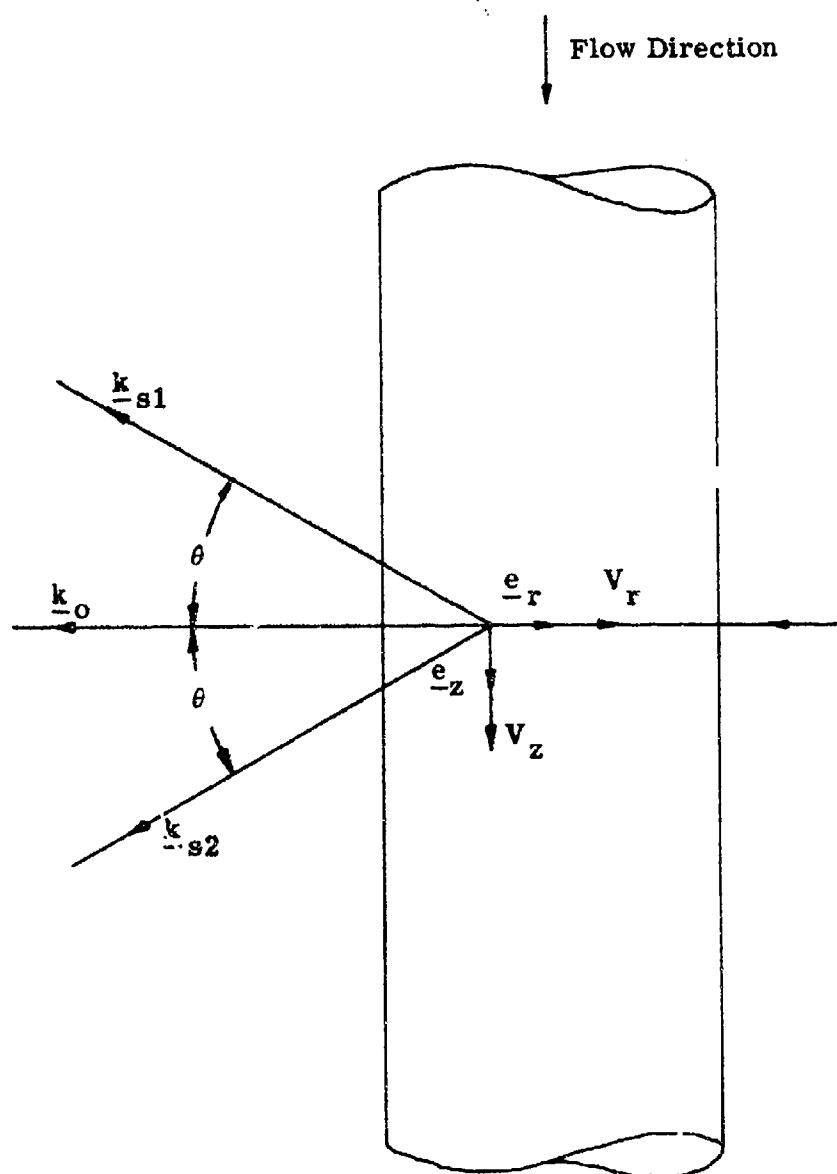


Figure 2.4

Optical Geometry for the Two-Component Laser-Doppler Anemometer



The relationship between the components of  $\underline{V}$  and the Doppler-shifted frequencies for our two-component optical geometry can be determined by considering equation (2.5) and Figure 2.4. The flow velocity  $\underline{V}$  in terms of the cylindrical coordinates defined in Figure 2.4 is

$$(2.6) \quad \underline{V} = V_r \underline{e}_r + V_z \underline{e}_z + V_\theta \underline{e}_\theta.$$

The direction of the incident beam is defined by the unit vector  $\underline{k}_0$

$$(2.7) \quad \underline{k}_0 = -\underline{e}_r.$$

The direction of a ray of laser light scattered through an angle  $\theta$  above the incident beam is defined by the unit vector  $\underline{k}_{s1}$ , where

$$(2.8) \quad \underline{k}_{s1} = -\cos \theta \underline{e}_r - \sin \theta \underline{e}_z.$$

Likewise the direction of a ray of laser light scattered through an angle  $\theta$  below the incident beam is defined by the unit vector  $\underline{k}_{s2}$ , where

$$(2.9) \quad \underline{k}_{s2} = -\cos \theta \underline{e}_r + \sin \theta \underline{e}_z.$$

The Doppler-shifted frequency,  $f_{d1}$ , in the  $\underline{k}_{s1}$  direction is, using equation (2.5)

$$\begin{aligned} f_{d1} &= \frac{f_0 \underline{V}}{C} \cdot (\underline{k}_{s1} - \underline{k}_0), \\ &= \frac{f_0}{C} (V_r \underline{e}_r + V_z \underline{e}_z + V_\theta \underline{e}_\theta) \cdot [(1 - \cos \theta) \underline{e}_r - \sin \theta \underline{e}_z], \end{aligned}$$

## Chapter III

### THE OPTICAL SYSTEM

The two most important parameters governing the performance of an experimental system are the signal to noise ratio, SNR, and the frequency response. In order to obtain a high over-all SNR in the laser-Doppler anemometer, the optical components must be carefully aligned in accordance with some stringent optical requirements. (These requirements will be developed in the next chapter.) The key to the operation of the LDA as a useful experimental tool is an optical bench that will permit easy alignment and adjustment of its components. The optical bench used in this work was designed and built at The University of Michigan in order to satisfy the optical requirements and also to offer ease of alignment and adjustment.

#### 1. Optical Arrangement

The optical arrangement used in this experiment (Figure 3. 1) was a variant of the one used by Goldstein and Kreid (1967). It can be briefly described as follows: the output beam of a Helium-Neon laser (beam  $B_0$  in Figure 3. 1) is split at beam splitter  $BS_1$  (10% reflection) into beams  $B_0$  and  $B_1$ . Beam  $B_1$ , a reference beam, is reflected at mirror  $M_1$  and focused at point 0 by means of lens  $L_1$ , where it forms an angle  $\theta$  with respect to beam  $B_0$ . After passing through point 0, beam  $B_1$  passes through the front aperture  $A_{f1}$ , the front receiving lens  $L_{f1}$ , pinhole  $P_1$ , the rear receiving lens  $L_{r1}$ , and the rear aperture  $A_{r1}$ ,



before striking photomultiplier P. M.  $_1$ . The reference beam  $B_1$  is optically heterodyned at the P. M. photocathode surface with the portion of the scattered beam front (from beam  $B_0$ ) allowed through apertures  $A_{f1}$  and  $A_{r1}$  and pinhole  $P_1$  to produce a signal at the P. M. whose frequency is the Doppler-shifted frequency. The output signal produced by the optics and P. M. along beam  $B_1$  is termed the output of channel 1.

Similarly beam  $B_2$ , a reference beam, is formed by beam splitter  $BS_2$ , (25% reflection), reflected at mirror  $M_2$  and focused by lens  $L_2$  at point 0 where it forms an angle  $\theta$  with beam  $B_0$ . Beam  $B_2$  then passes through aperture  $A_{f2}$  lens  $L_{f2}$ , pinhole  $P_2$ , lens  $L_{r2}$ , and strikes P. M.  $_2$  after passing through aperture  $A_{r2}$ . Beam  $B_2$  is heterodyned at the P. M. with a portion of the scattered wave to produce another Doppler-shifted signal. The output signal produced by the optics and P. M. along  $B_2$  is termed the output of channel 2. After the beam splitter  $BS_2$ , beam  $B_0$ , the scattering beam, passes through lens  $L_0$  which focuses it at point 0 where it is scattered. The trisection of beams  $B_0$ ,  $B_1$ , and  $B_2$  at point 0 forms the measuring volume.

## 2. Optical Geometry

The optical geometry can be described as follows: Beam  $B_0$  was aligned so as to be perpendicular to the outside faces  $F_1$  and  $F_2$  of the test section and to pass through the axis of flow, D. Beams  $B_1$  and  $B_2$  were placed at equal angles  $\theta$  on either side of beam  $B_0$  and lay in the

plane formed by the axis D and beam  $B_0$  and intersected at point O. This choice of optical geometry provided an easy method of obtaining the axial and radial components of velocity. (In the same way as one obtains these quantities from the output of a X-wire in hot-wire anemometry.) This configuration further minimized optical distortion due to the presence of the test section. This geometry, a two-component variation of the one used by Goldstein and Kreid (1967), offered an additional advantage over the geometries used by Foreman et al (1966) and Rolfe et al (1968) in that the optical mixing of the scattered and reference beams in the present system took place at the measuring volume rather than at the P.M. Therefore, beam alignment became less critical.

### 3. Optical Components

All of the optical components, lenses, mirrors, photo multiplier tube holders, and the laser, were mounted on a vertical rigid reference plate, 14 inches high by 66 inches long. This plate was formed from 1/8 inch thick steel plate to the above dimensions with 1 3/4 inch flanges top and bottom. The rigidity of the plate was increased by welding a 2 1/2 x 2 1/2 x 66 inch angle iron along its length, 7 1/2 inches up from its base. The plate was mounted to a 300 pound 21 by 31 inch granite surface plate by means of four triangular braces and eight screws. The resulting reference plate-surface plate system was thus very rigid.

In order to obtain measurements across the test section, point 0, the measured point, (Figure 3. 1) must be moved relative to the test section. This was accomplished by a set of six rollers, placed between the granite table and the bench. Translation of the measuring point was accomplished by means of a spring loaded screw, one end mounted to the bench, the other to the granite table. (See Figure 3. 1) This allowed the entire optical system (and therefore point 0) to be moved as a unit. The transverse position of the measuring point 0 in the test section was determined by first locating it visually (using a telescope) at the pipe center. Subsequent positions were determined by reading a dial indicator placed against the granite table in the line of motion. Due to the refraction of the beams by the test section, the distance point 0 moved in the test section was  $4/3$  of the dial indicator movement. (Details of the refractive effect of the test section on beam geometry can be found in Appendix A.)

The bench mentioned above consisted of 1 1/2 inch plywood mounted on Unistrut supports which were in turn mounted on a cement block base. Asphalt saturated felt was placed between the cement blocks to isolate the optical bench from building vibrations.

The test section was machined from a solid piece of 3. 125 by 3. 125 by 4 inch Plexiglas (Index of refraction 1.5). A two inch hole was machined through the center of the square cross section. It was recessed at either end to fit smoothly into the two inch internal diameter brass pipe to which it was attached by flanges. The optical surfaces of the

test section were polished to a scratch-free finish by means of successive applications of Bon-Ami and Cadco Anti-Static polish.

The inner surface of the test section was cleaned periodically of a build-up of dirt, latex, and polymer to avoid impairment of its optical qualities. This cleaning was accomplished by removing the lower flange from the test section so that the inner surface could be cleaned with Cadco Anti-Static polish. The polish was applied with lint-free cotton balls on the end of a dowel rod.

The laser (Spectra-Physics Model 120, Helium-Neon laser, wavelength 6328 angstroms) was mounted on an I-beam which was attached rigidly to the vertical steel reference plate. The mounting holes in the I-beam were slotted to allow adjustment of the laser to pass through the center of the test section and also to be perpendicular to its outer surfaces.

The front surface mirrors used in this experiment were mounted in hemi-spherical holders. These holders were attached firmly to the mirror mounts with magnets. The mirror mounts were then attached to the reference plate by slotted bars and held in position by knurled tightening nuts. (See Figure 3.2) The slotted bars allowed for gross translation in two dimensions. The mirror mount could be fine adjusted in one direction by means of a screw operated, spring loaded translation stage. This, along with the two degrees of rotational freedom allowed by the hemi spherical mirror holders, permitted easy mirror adjustment.

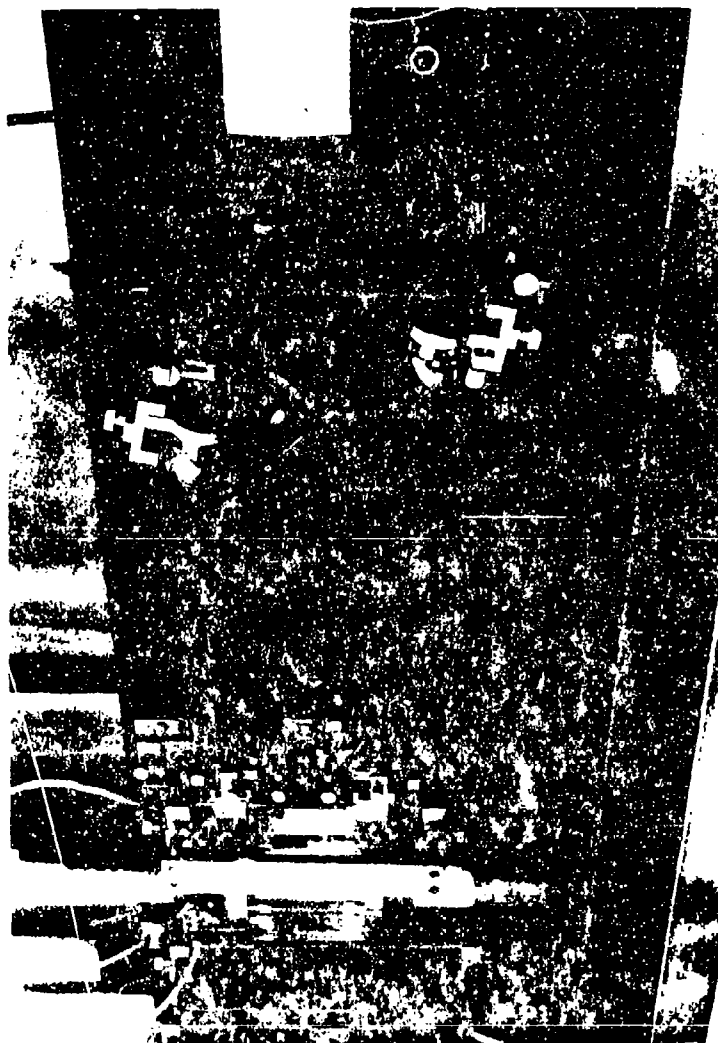


Figure 3.2  
Transmitting Optics

Reproduced from  
best available copy.





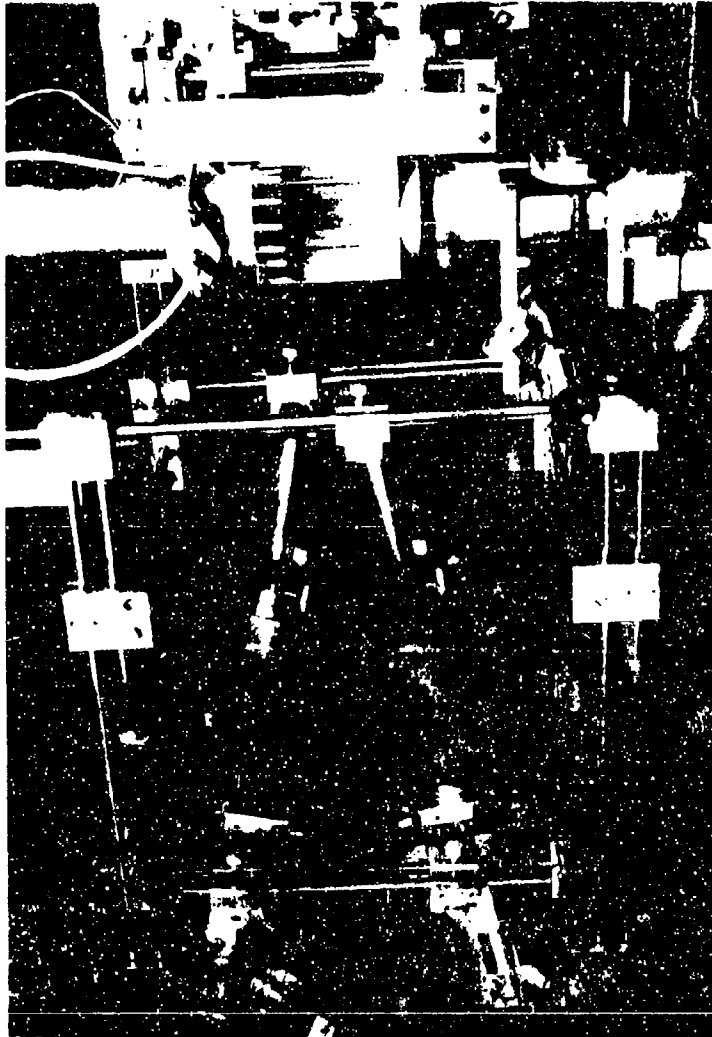


Figure 3.3  
Receiving Optics

The beam splitter holders were mounted perpendicular to the reference plate by a sleeve attached to the plate. (See Figure 3.2.) The angle between beam splitter holder and beam could be adjusted by rotating the holder pin in the sleeve. It was held in place by a knurled tightening nut. Fine angular adjustment of the beam splitter was accomplished by adjusting the set screws located in the holder.

The lens holders were mounted on a slide array which allowed for gross translation in the three coordinate directions. The slide array, which was mounted to the reference plate, consisted of a series of spring-loaded blocks mounted on drill rod as shown in Figure 3.2. The lens holders were mounted on several blocks of the same design. The lens holders themselves could be fine adjusted in two coordinate directions by screw operated, spring-loaded translation stages (similar to those used in the mirror mounts). A yoke mechanism provided an additional two degrees of rotational freedom. These adjustments were found sufficient for accurate lens placement and alignment.

The photomultiplier tube holder mounts were attached to the reference plate on one side and to the supporting table, with vertical rods, on the other side. (See Figure 3.3) This mechanism allowed for gross translation of the P.M. holders in the three coordinate directions utilizing the same type of slide array design used in the lens system. Yokes mounted on the front of the slide array allowed for rotation in two directions about the leading aperture,  $A_{f1}$ , in the P.M. holder. A yoke mechanism mounted on the rear slide array likewise provided

the rotation about two coordinate axis needed for gross alignment of the P.M. holders. Finally, spring-loaded screw adjustable adjustment frames mounted on the rear slides provided fine angular adjustment of the P.M. holder about the leading aperture.

The P.M. holder (see Figure 3.3) housed the P.M. tube as well as the apertures  $A_f$  and  $A_r$  and the lens-pinhole combination of  $L_f$ ,  $L_r$  and P. The apertures, which were adjustable, prevented extraneous light from reaching the P.M. tube. They also provided an easy reference for aligning the P.M. holder along the beam axis as well as providing a means to block-off the unwanted portion of the reference beam. The pinhole-lens combination (suggested by F. Danel) was designed so that the image of the measuring point 0 was projected on the P.M. tube. The pinhole diameter was the same size as the measuring volume cross-section. Therefore, any light extraneous to the measuring volume was cut-off by the pinhole. Thus the P.M. "saw" only the measuring volume and the error due to sensing velocities from other points was minimized. This became especially important when making measurements close to reflecting boundaries. This design was instituted when it was found that the heterodyned signal was too "noisy" when the measuring volume was close to the pipe wall. The pinhole-lens combination was mounted as a unit and could be moved along the P.M. holder axis by means of a spring-loaded adjusting screw. This, along with the adjustable bushing adapter (see below)

allowed the pinhole-lens combination to be adjusted to produce the best signal.

The main body of the P.M. holder was made from two sizes of copper tubing which also served as an effective electrostatic and magnetic shield (see Figure 3.3).

The P. M. holder was completely light-sealed and had a cover which fit over the front aperture to prevent background light from entering and fatiguing the P.M. tube when the LDA was not in operation. The inside surfaces of the holder were painted ultra-flat black to absorb any stray light.

The P.M. tube socket was contained in a housing along with the voltage-dividing circuitry for the P.M. tube. The housing had B.N.C. connections for input from the power supply and output to the readout unit. (This output was the heterodyned signal.) The housing slid into a bushing adapter which in turn slid into the P.M. holder. The bushing adapter could be moved along the P.M. holder axis so that the P.M. front-surface-to-lens  $L_r$  distance could be varied. The P.M. tube and circuit assembly were held in place in the P.M. holder with set screws. This allowed for easy removal of the assembly to allow adjustment of the P.M. holder during alignment.

All reflecting surfaces of the optical bench were painted ultra-flat black to minimize the incidence of stray light. Furthermore, the entire optical bench was housed in a light-sealed room to isolate it from the main laboratory area.

## Chapter IV

### SIGNAL-TO-NOISE CONSIDERATIONS FOR THE LASER-DOPPLER ANEMOMETER

The laser-Doppler anemometer uses the proportionality of the Doppler-shifted frequency of the scattered wave to the fluid velocity at the measuring point to make flow measurements. The anemometer used in this experiment, described previously, mixed the Doppler-shifted scattered wave with a reference wave of the initial unshifted frequency at the measuring point, 0. The resulting wave was sensed by a photomultiplier tube (RCA 7326). The photomultiplier can be operated in two modes; as a detector (low level) of electromagnetic waves or as a mixer of electromagnetic waves, as in the present experiment. As used in the current work, the photomultiplier acted as a superheterodyne receiver. In this mode of operation of the P.M., the frequency of the incoming Doppler-shifted signal was mixed with that of the unshifted reference signal (local oscillator) to a new, lower, frequency. This signal was then amplified before further processing was done by instrumentation subsequent to the P.M. The P.M. possesses advantages over other sensing devices in that it offers an essentially noiseless post detection gain. Furthermore, the bandwidth of the P.M. allows measurement of velocities into the supersonic range, far beyond the needs of this experiment.

### 1. Noise in the P. M. Tube

Noise in the P.M. tube is generated by random electron motion. Its spectrum is flat, i.e., the noise is white. The three dominant noise sources are: (1) Dark current. When the P.M. is operated in the absence of incident light, an anode current flows which sets a limit to the lowest intensity of light that can be measured. It is caused mainly by thermionic current emitted from the photosensitive coating. (2) When light impinges on the P.M. tube, the output noise increases significantly because of statistical fluctuations of the photoemission current modified by the gain variation of the multiplier. This is called shot noise or "noise-in-signal" since it is a function of the input signal. (3) Shot noise contributed by extraneous light (light from sources from other than the measuring volume) (Rolfe et al, 1968).

The noise from background light can be minimized by placing apertures in front of the P.M. tube to block off this light. The dark current is negligible in comparison to the current due to the incident laser beam light. Therefore, the dominant noise source which limits the sensitivity of the LDA is the noise in the signal.

### 2. Noise in the Signal

The two most important parameters governing the sensitivity of an instrument are its signal-to-noise ratio and its bandwidth (frequency response). In this section an expression for the signal-to-noise ratio (SNR) for the P.M. tube is developed.

The first step in this development is to calculate the P.M. anode current.

Consider two light beams incident on the photocathode surface:  $E_s \sin w_s t$  due to the scattered radiation and  $E_r \sin w_r t$  due to the reference radiation, where  $E$  denotes the electric field amplitude and  $w$  is the radian frequency of the light. These waves add to become the total incident radiation at the cathode whose electric field is

$$(4.1) \quad E_t = E_s \sin w_s t + E_r \sin w_r t ,$$

assuming the beams have the same linear polarization direction.

Since the P.M. is a square law detector, the anode current output is proportional to the power of the incident light beam

$$(4.2) \quad I_{ta} = S E_t^2 = S [E_s^2 \sin^2 w_s t + E_r^2 \sin^2 w_r t + 2E_r E_s \sin w_r t \sin w_s t] ,$$

where the current amplification  $S$  is assumed constant. This can be rewritten as

$$(4.3) \quad I_{ta} = S \left\{ E_s^2 \left( \frac{1}{2} - \frac{\cos 2 w_s t}{2} \right) + E_r^2 \left( \frac{1}{2} - \frac{\cos 2 w_r t}{2} \right) + E_r E_s [\cos (w_s - w_r) t - \cos (w_s + w_r) t] \right\} .$$

The terms containing the frequencies  $2w_s$ ,  $2w_r$ , and  $(w_s + w_r)$  are not important since they fall outside the bandwidth of the P.M. Therefore,

$$(4.4) \quad I_{ta} = S \left\{ \frac{E_s^2 + E_r^2}{2} + E_s E_r \cos(w_s - w_r) t \right\}$$

or

$$(4.5) \quad I_{ta} = S_k \{ P_s + P_r + 2\sqrt{P_s P_r} \cos \Delta w t \} ,$$

where  $P$  is the light power impinging on the photocathode,  $\Delta w$  is  $w_s - w_r$ , and  $S_k$  is the cathode radiant sensitivity. This is the total current emitted by the cathode in response to the laser light.

The noise current,  $i_k$ , is given by the shot noise equation

$$(4.6) \quad i_k^2 = 2e \Delta f I_{ta} ,$$

$$(4.7) \quad i_k^2 = 2e \Delta f S_k [P_s + P_r + 2\sqrt{P_s P_r} \cos \Delta w t] ,$$

where  $e$  is the electron charge. This represents the noise current spread randomly over the frequency range of bandwidth  $\Delta f$ . This noise can be measured by measuring its power,

$$\langle i_k^2 \rangle R ,$$

where  $i_k^2$  is the mean square noise current and  $R$  is the resistive component of the circuit impedance. Then

$$(4.8) \quad \langle i_k^2 \rangle = 2e \Delta f S_k (P_s + P_r) ,$$

where we have averaged  $i_k^2$  to get the mean square noise current.

The a.c. current at the cathode is, as we have seen

$$(4.9) \quad I_{ac} = 2S_k \sqrt{P_s P_r} \cos \Delta w t .$$



The mean square of the signal current is

$$(4.10) \quad \langle I_{ac}^2 \rangle = 2S_k^2 P_s P_r ,$$

and the cathode SNR is

$$(4.11) \quad \frac{\langle I_{ac}^2 \rangle}{\langle I_k^2 \rangle} = \frac{S_k P_s P_r}{e \Delta f (P_s + P_r)} .$$

The signal-to-noise ratio at the anode becomes

$$(4.12) \quad \left(\frac{S}{N}\right)_a = \frac{1}{k} \left(\frac{S}{N}\right)_c = \frac{S_k P_s P_r}{e \Delta f k (P_s + P_r)} ,$$

where

$$k = \frac{\sigma}{\sigma - 1} ,$$

$\sigma$  being the average gain per stage of the multiplier chain.

Rewriting equation (4.12) we have,

$$(4.13) \quad \left(\frac{S}{N}\right)_a = \frac{S_k}{e \Delta f k} P_s \frac{1}{1 + \frac{P_s}{P_r}} .$$

We see that making  $P_r \gg P_s$  will maximize the SNR until, in the limit as  $P_r/P_s$  approaches infinity,

$$(4.14) \quad \left(\frac{S}{N}\right)_a = \frac{S_k}{e \Delta f k} P_s .$$

For this limiting case the SNR is seen to be independent of  $P_r$ .

However,  $P_r$  cannot be increased without limit.  $P_r$  is restricted in value such that  $I_{ta}$  (see equation (4.5)) does not exceed its maximum value as defined by manufacturer specifications.

### 3. Optical Loss Coefficients

The preceding derivation of the SNR did not take into account losses due to the optical system. These can be included by modifying equation (4.13) by introducing loss coefficients in the following manner,

$$(4.15) \quad \left(\frac{S}{N}\right)_a = C_d C_t C_c \left[ \frac{S_k}{e \Delta f k} P_s \frac{1}{1 + \frac{P_s}{P_r}} \right],$$

where

$C_d$  = P.M. alignment coefficient,

$C_t$  = Transmission path coherence loss factor,

and

$C_c$  = Source coherence length factor.

Since each of these effects tends to degrade the SNR, their coefficients must be less than or equal to one.

The source coherence length,  $L$ , a parameter that defines the coherence properties of a light source, is defined as that distance between two wave packets emanating from the same source such that their phase difference is  $\Delta\phi$ .

Born and Wolf (1964) present an expression for source coherence length for  $\Delta\phi = 2\pi$ ,

$$(4.16) \quad L = C / \Delta\nu,$$

where  $\Delta\nu$  is the frequency spread and  $C$  the free space velocity of light.

The source coherence length for lasers is on the order of  $(10)^6$  feet. Therefore, for the present experiment, the source coherence factor,  $C_c$ , is essentially unity.

In their passage from laser to P.M., the laser beams may be degraded in such a way as to affect their ability to produce coherent heterodyne signals at the P.M. The two causes of this degradation are: (1) fluctuations in effective path length due to fluctuations in path density and therefore refractive index and wavelength; and by fluctuations in geometrical path length with bent rays; (2) scattering from atmospheric or other sources outside the measuring volume (Rolfe et al, 1968). One measure of these effects is the transmission path coherence length. If the difference between the effective beam lengths of the various beams used in an experiment is less than the transmission path coherence length, coherent heterodyning will be possible. Since the beam lengths of the current work differed by less than 4 inches, the transmission path coherence length for this optical system, no coherence problem was encountered.

Due to errors in the optical mixer (P.M.) geometry and alignment with respect to the incoming beams, the SNR can be attenuated significantly by an amount  $C_d$ .

In this experiment, alignment problems arose due to angular mismatch between the incoming beams and the P.M. cathode face and also due to unwanted beam overlap on the cathode face between the scattered and reference beams.

Rolfe et al (1968) have shown that the angular alignment between beams and the P.M. surface is not critical. Furthermore, the P.M. tube holders and their mounts used in this work were designed to minimize this problem.

That portion of the reference beam that does not intersect the scattered beam on the P.M. cathode face induces shot noise without increasing the signal strength. Consequently, this reference beam overlap reduces the SNR significantly. To avoid this problem, apertures and a pinhole were placed in front of the P.M. to block-off the unwanted portion of the reference beam.

The optical geometry used in the current work offered some distinct advantages over those used by other investigators. In the geometries used by Rolfe et al (1969) and Foreman et al (1965), mixing of scattered and reference beams took place on the P.M. tube photocathode surface necessitating careful alignment to avoid angular mismatch between the beams. Any beam mismatch would degrade the SNR. This problem did not arise in the current work since the scattered and reference beams mixed at their point of intersection (point 0 of Figure 3.1). Alignment of the P.M. was then effected by merely aligning the P.M. holder so that the reference beam passed through the apertures at their smallest diameter.

A further advantage of the geometry used here is that beam size, on the P.M., was immaterial.

It might be well to mention here that the laser anemometer proposed by Rudd (1969) possesses further advantages. This device, which could be termed an interference-fringe anemometer as it does not use the Doppler principle, has the same mathematical relationship between detected frequency and flow velocity as the LDA. The velocity at the measuring volume is detected as the ratio of the distance between interference fringes and the time it takes for a particle to pass between them. The interference fringes occur at the measuring volume and are produced as follows (see Figure 4.1): Light from a high power laser is diverged by lens  $L_1$  to cover the mask M. This light is focused by a single lens  $L_2$  to point O in the fluid. Since both beams pass through the same lens,  $L_2$ , they are brought to focus, and therefore overlap, at the same point O. This system is truly self-aligning. An interference fringe pattern is formed at the point O due to the interaction of the two beams of equal intensity that intersect there. After passing through the fluid, the beams are focused by lens  $L_3$  on a photo detector. The output of this detector is a voltage whose frequency is related to the velocity at the measuring volume in the same way that the Doppler frequency is in the LDA.

Not only does this system provide ease of alignment, but the frequency shift is independent of detector position. This implies that there is no aperture broadening. (Aperture broadening will be discussed later in this chapter.)

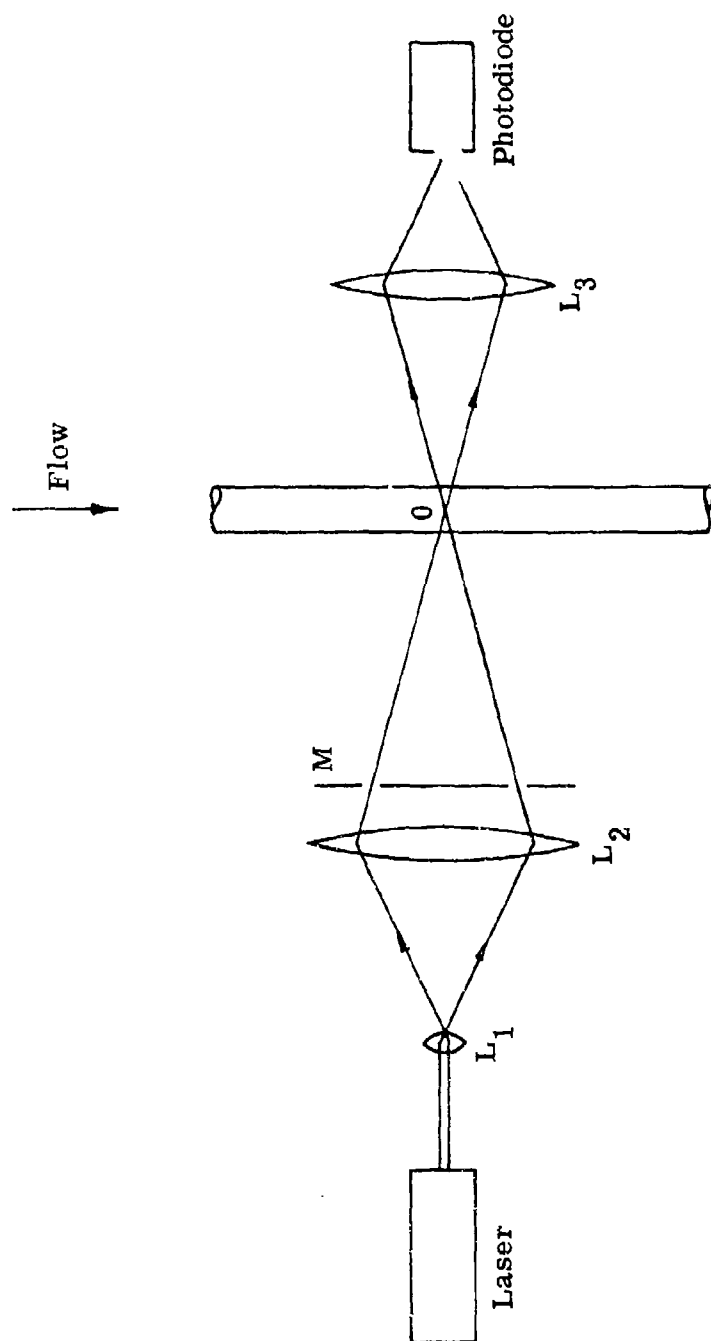


Figure 4. 1  
Optical Arrangement of Rudd (1969)

With all of these advantages, the interference-fringe anemometer seems to be a promising form of laser anemometer. It does have the disadvantage, however, of requiring greater laser power with the attendant safety problems.

#### 4. Instrumental Broadening

The frequency spectrum of the laser light of a LDA will be broadened (departing from purely monochromatic light) due to several physical processes:

- (1) turbulence phenomena,
- (2) finite aperture size,
- (3) finite measuring volume size..

The frequency of scattered light from a flowing fluid is sensitive to flow fluctuations as seen from the relationship developed in Chapter 2,

$$(4.17) \quad f_d = \frac{f_o}{C} \underline{V} \cdot (\underline{k_s} - \underline{k_o}) .$$

Since turbulence is a random phenomenon, that is, it is characterized by random fluctuations of velocity about some mean velocity, it is seen from equation (4.17) that the frequency of the Doppler-shifted light varies randomly about a mean (is broadened).

Anything that would obscure these turbulent fluctuations (broadening from other sources) would reduce the sensitivity of the LDA. Such undesirable broadening is induced because of the finite size of

receiving aperture and pinhole diameters and because of the finite size of the measuring volume. These effects will be discussed below.

Consider the optical geometry of Figure 4.2. From equation (4.17), the Doppler-shifted frequency,  $f_d$ , is

$$(4.18) \quad f_d = \frac{2V}{\lambda} \sin \theta .$$

Therefore

$$(4.19) \quad \frac{\partial f_d}{\partial \theta} = \frac{2V}{\lambda} \cos \theta .$$

Now, if  $R$  is the distance between the aperture and measuring point and  $r$  the aperture radius, the incremental angular uncertainty,  $\Delta \theta$ , can be written as

$$(4.20) \quad \Delta \theta = \frac{2r}{R} .$$

The aperture broadening is

$$\Delta f_a = \frac{\partial f_d}{\partial \theta} \Delta \theta = \frac{2V}{\lambda} \Delta \theta \cos \theta ,$$

$$(4.21) \quad \Delta f_a = \frac{4Vr}{\lambda R} \cos \theta .$$

For this experiment the aperture broadening was

$$\Delta f_a \approx (10)^4 \text{ HZ} .$$

This was a tolerable level for the present experiment since  $f_d$  for the centerline velocity was about  $(10)^5$  HZ at a Reynolds' number of 50,000. However, this broadening must be compared with the natural broadening due to the turbulent fluctuations.



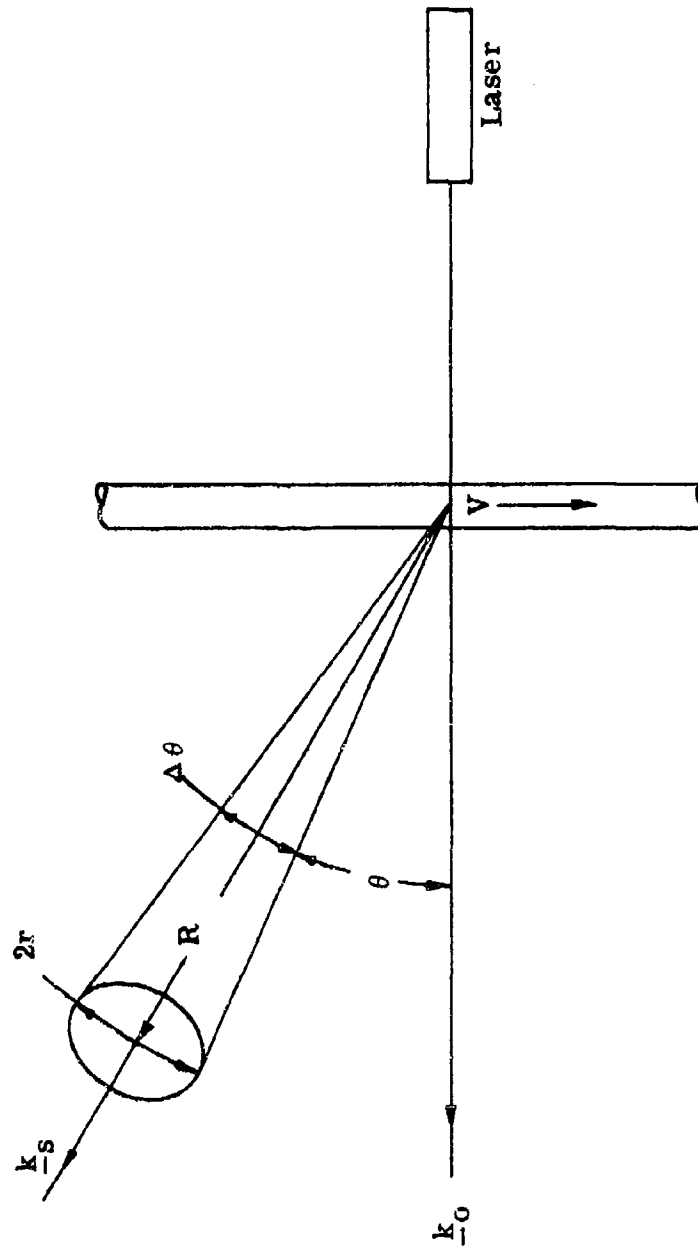


Figure 4.2  
Geometry of Aperture Broadening

The stream velocity  $\underline{V}$  at a point in the flow can be written as

$$(4.22) \quad \underline{V} = \underline{\bar{V}} + \underline{V}'$$

where  $\underline{\bar{V}}$  is the mean velocity, a constant in time, and  $\underline{V}'$  is the variation of velocity about that mean.

Equation (4.22) can be written in scalar form as

$$(4.23) \quad V_z = \bar{V}_z + V'_z ,$$

$$(4.24) \quad V_r = \bar{V}_r + V'_r ,$$

where  $z$  and  $r$  denote the axial and radial components respectively and we are not considering the swirl component of velocity.

Recall that

$$(4.25) \quad f_{dz} = (f_{d2} - f_{d1}) = \frac{2}{\lambda} V_z \sin \theta ,$$

$$(4.26) \quad f_{dr} = (f_{d2} + f_{d1}) = \frac{2}{\lambda} V_r (1 - \cos \theta)$$

and noting that the mean velocities and fluctuations satisfy these equations independently,

$$(4.27) \quad \frac{\partial f_{dz}}{\partial V'_z} = \frac{2}{\lambda} \sin \theta ,$$

and

$$(4.28) \quad \frac{\partial f_{dr}}{\partial V'_r} = \frac{2}{\lambda} (1 - \cos \theta) .$$

The broadening due to the axial fluctuations is

$$(4.29) \quad \Delta f_z = \Delta V'_z \frac{\partial f_{dz}}{\partial V'_z} = \frac{2}{\lambda} \Delta V'_z \sin \theta ,$$

which for this experiment was

$$\Delta f_z \approx (10)^5 \text{ HZ}.$$

Similarly, the broadening due to the radial fluctuations is

$$(4.30) \quad \Delta f_r = \frac{2}{\lambda} \Delta V'_r (1 - \cos \theta)$$

which for this work was

$$\Delta f_r \approx (10)^4 \text{ HZ}$$

Thus the axial turbulent fluctuations were essentially unaffected by aperture broadening, whereas the radial fluctuations were of the same order of magnitude as the aperture broadening.

The broadening due to a finite size measuring volume is

$$(4.31) \quad \Delta f_v = \frac{\partial f_{dz}}{\partial V_z} \Delta U_z = \frac{\partial f_{dz}}{\partial V_z} \frac{\partial V_z}{\partial r} \Delta r$$

From equation (4.25)

$$(4.32) \quad \frac{\partial f_{dz}}{\partial V_z} = \frac{2}{\lambda} \sin \theta.$$

Here  $\Delta r$  is just the effective depth of focus of the receiving lens combination of  $L_f$  and  $L_r$ , of Figure 3.1. The depth of focus is related to the wavelength  $\lambda$  and the lens number,  $F$ , by

$$(4.33) \quad \Delta r = 4F^2 \lambda,$$

where the lens number is equal to the lens focal length divided by the aperture size. Therefore

$$(4.34) \quad \Delta f_v = 8 \sin \theta F^2 \frac{\partial V_z}{\partial r}.$$

Thus, measuring volume broadening becomes strongest in the region of the steepest velocity gradient which, for this experiment, was near the wall.

The effect of finite measuring volume size can be minimized by making the lens number of the receiving lens as small as possible.

## Chapter V

### FLOW SYSTEM

#### 1. Description of the Flow System

The flow system used in this experiment is shown in Figure 5.1. The system can be described as follows: Water from the city water supply entered through valve  $V_1$  and passed through a turbine flow meter. The flow rate was proportional to the resulting output frequency which was monitored on a frequency counter.

The polymer was injected into an elbow near the mixing tank inlet. The resulting dilute polymer solution passed through a honeycomb straightener and entered a two inch brass pipe via a rounded inlet at the bottom of the mixing tank. The scattering particles were injected just beyond this inlet by a piston pump which was driven by air pressure.

The pressure drop in the brass pipe was measured by an inclined U-tube manometer attached to sidewall pressure taps located 11.875 feet apart.

The fully developed flow passed through the test section (220 diameters from the pipe inlet), through the flow control valve,  $V_2$ , and out the drain.

A single-pass flow system was chosen rather than a closed loop system to avoid mechanical degradation of the polymer solution and to provide a freshly mixed solution.

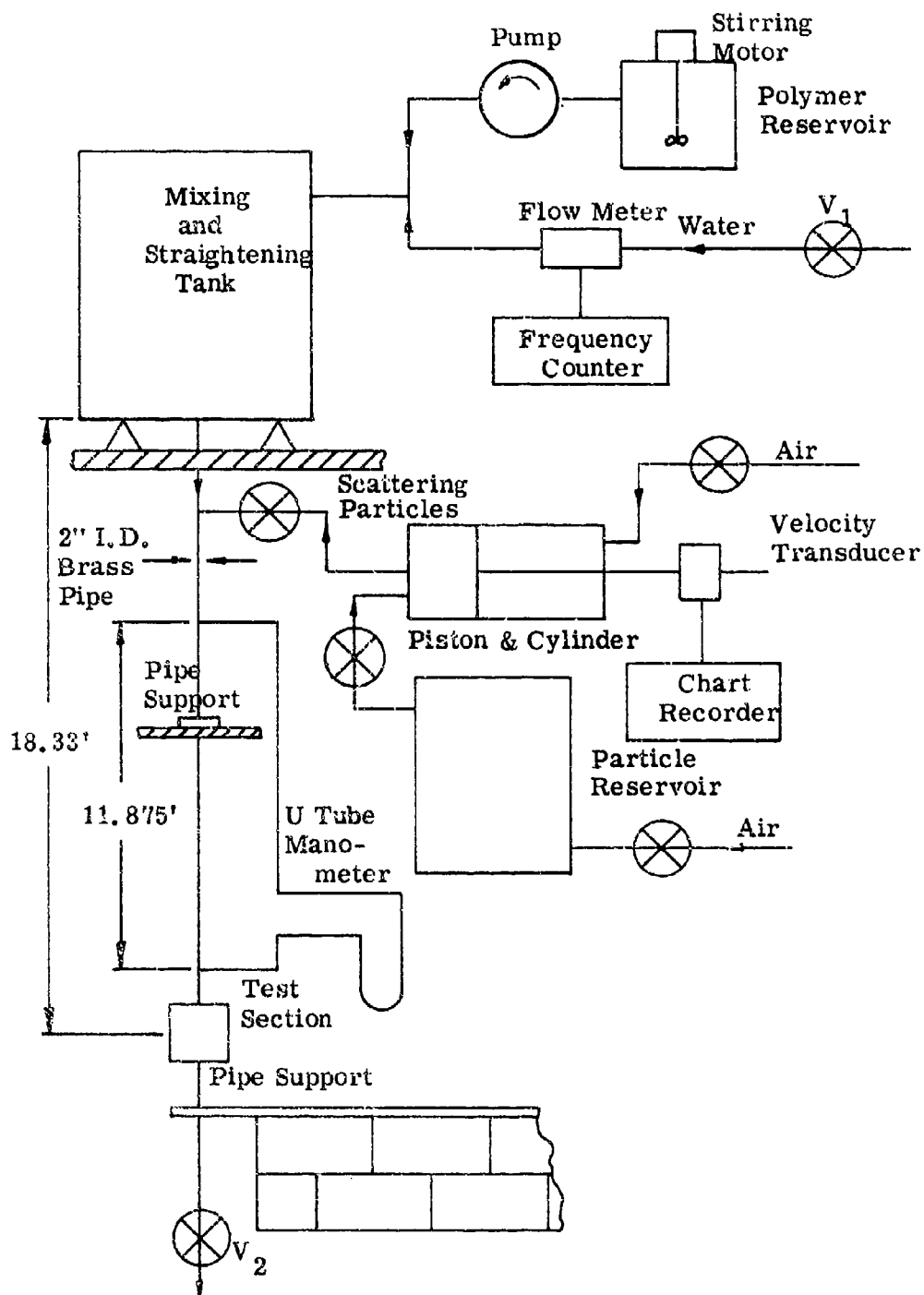


Figure 5.1  
Flow System

## 2. Polymer Injection

The usual method of preparing a polymer solution from the polymer powder consists of preparing a master batch which is diluted to the desired polymer concentration. Since water soluble polymers dissolve slowly and have a tendency to clump, this process can be tedious and time consuming. Furthermore, since the solutions are usually prepared well in advance of use, degradation due to aging is introduced.

To avoid these problems, the polymer was injected as a powder into the water flow. This injection was accomplished by pumping a slurry of polymer powder in methanol into the water flow. Uniform concentration of the polymer-methanol solution was assured by continuously stirring it in the reservoir. Since methanol is a non-solvent of Separan AP30 (the polymer used), there was no chance for clumping to occur. The pump used was a variable speed tubing pump that was regulated to compensate for changes in torque or system pressure to assure a constant flow rate.

The resulting polymer-water solution was quite fresh albeit perhaps of non-uniform concentration due to the presence of macroscopic lumps of high concentration polymer. It was hoped that this non-homogeneous concentration would produce a variation of the drag reduction phenomena usually observed.

The polymer used was a polyacrylamide (Separan AP30). This type of polymer is a good drag-reducing agent, and is also less susceptible

to shear degradation than polyethylene oxides, which are also good drag reducing agents.

### 3. Scattering Particles

Particle contaminants must be present in the flow in order to generate a Doppler-shifted light wave through light scattering. Yeh and Cummins (1964), in their pioneering work on the LDA, showed that coherent mixing is possible using light scattered from uniform sized polystyrene particles. Later, Foreman et al (1965) showed that optical heterodyning is possible using scattering particles of irregular size and shape.

Natural contaminants cause sufficient scattering for heterodyning, when using high-power lasers. Since a 5 mw laser was used in this work, it was decided to use polystyrene particles of uniform size (average diameter 0.2 microns) as the scattering medium. These particles are sufficiently small as well as being practically neutrally buoyant, so that they do not alter the flow (Huffaker, 1970). This is important since the velocity measured by the LDA is the scattering particle velocity. The concentration in the scattering volume was high enough to prevent a significant drop-out in the heterodyned signal.

The cost of commercially available polystyrene particles in the quantities needed is prohibitively high. Therefore, it was decided to manufacture them from raw styrene using a technique developed by



Woods, Dodge, and Kriger (1968). The particles so produced have been found suitable for our purposes.

The scattering particles were injected into the flow just below the accumulator tank using a piston (see Figure 5.1). The piston was driven using air pressure. A velocity transducer measured the piston speed, thus enabling calculation of the scattering concentration provided the water flow rate and the particle concentration in the cylinder were known also.

The optimal concentration was determined by varying the particle flow from the cylinder and observing the effect on the quality of the heterodyned signal as seen on an oscilloscope. By this means, the particle concentration was chosen to be  $2(10)^{-3}$  % by weight. This is the same concentration used by Chu and Schoenes (1968) in their work.

## Chapter VI

### SIGNAL PROCESSING

#### 1. Readout Unit

To obtain the mean velocity and turbulence intensity profiles of the axial and radial components in a pipe flow, one must be able to extract the mean frequency and the fluctuations about it from the time varying Doppler frequency output of the P.M. Several investigators have used spectrum analyzers to do this (Goldstein and Kried, 1967; Rudd, 1972). Unfortunately, one cannot obtain the energy spectra or Reynolds' stresses using this signal processing technique.

Others (Foreman et al, 1965; Fridman, Kinnard, and Meister, 1969) have developed a variety of signal processing devices to extract the mean and fluctuating frequencies from the P.M. output signal. These units have the advantage of yielding an output proportional to the instantaneous velocity fluctuations, thereby allowing processing to obtain energy spectra and Reynolds' stress.

The unit used in this work was a model MFT 100 X readout unit made by Electronics, Inc. It has the capability of measuring the mean Doppler frequency as well as the time varying fluctuations about the mean. This unit has a frequency response of 50 KHZ to 10 MHZ which was found sufficient for this experiment.

Referring to Figure 6.1, the readout unit circuitry can be described as follows: the output of the P.M. tube (the heterodyned signal) is fed into the input jack of the readout unit. From here it goes into a low

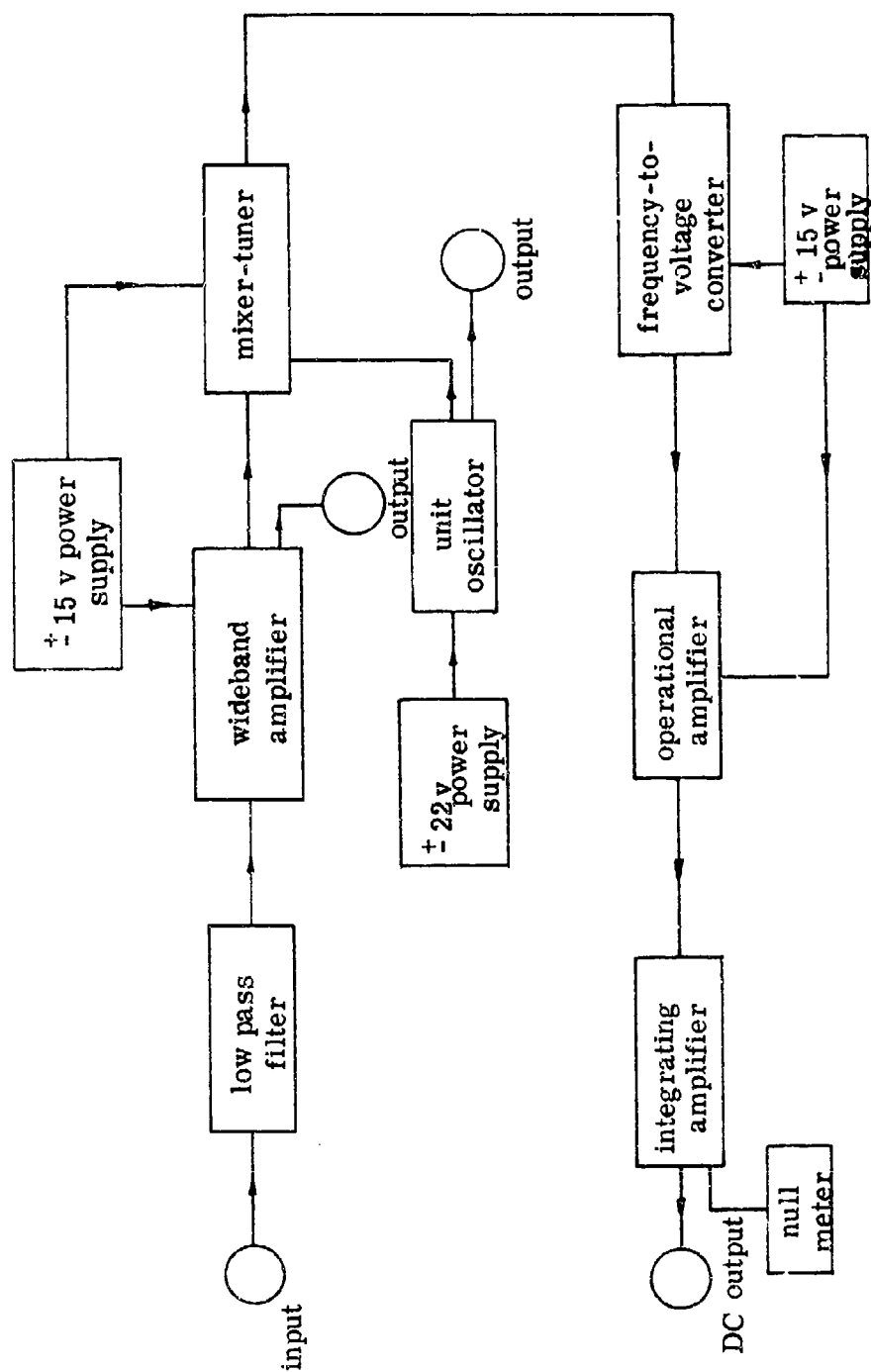


Figure 6.1  
Readout Unit Circuitry

pass filter (10 MHz cut-off) and is then amplified in a wideband video amplifier. The amplifier output goes to a front panel jack so that the signal may be viewed on an oscilloscope. Its output also goes to a mixer-tuner where it is heterodyned with the unit oscillator signal. The resulting signal is fed into a frequency-to-voltage converter which yields a voltage proportional to the difference frequency. After several stages of amplification, the signal is fed into a front panel jack, and also to a front panel null meter. The unit oscillator frequency is adjusted until the meter indicates a null. This frequency represents the mean velocity. The output signal is then proportional to only the turbulent part of the velocity.

## 2. Signal Processing Set-Up

The instantaneous velocity of a turbulent flow is considered to be the sum of a time-invariant mean velocity and a velocity fluctuating about this mean, that is,

$$(6.1) \quad \underline{V}(t) = \underline{\bar{V}} + \underline{V}'(t) .$$

Recalling the frequency-velocity relation developed in Chapter 2

$$(6.2) \quad f_d = \frac{f_d}{C} \underline{V}(t) \cdot (\underline{k}_s - \underline{k}_o) ,$$

we see that  $\underline{\bar{V}}$  and  $\underline{V}'(t)$  each satisfy the above equation independently.

Similarly the components of  $\underline{\bar{V}}$  and  $\underline{V}'(t)$  individually satisfy the component frequency velocity relations

$$(6.3) \quad V_z(t) = \frac{C}{f_o} \left( \frac{f_{d1} - f_{d2}}{2 \sin \theta} \right)$$

and

$$(6.4) \quad V_r(t) = \frac{C}{f_o} \left( \frac{f_{d1} + f_{d2}}{2(1 - \cos \theta)} \right) .$$

Keeping these equations in mind, let us consider the signal processing set-up shown in Figure 6.2. The output of the P.M.s feed into their respective readout units. Each unit oscillator can be adjusted so as to produce a null as indicated by a D.C. voltmeter attached to the output of the readout. The frequencies of the unit oscillators at this setting are the mean Doppler frequencies and therefore yield the mean axial velocity through equation (6.3). The fluctuating voltages from the unit outputs are added and subtracted from the input signals to yield outputs related to the fluctuating components of velocity (see equations (6.3) and (6.4)). The outputs of this unit can be taped for later wave analysis, fed into RMS meters to obtain turbulence intensities, and also multiplied and read on a D.C. voltmeter, the result being proportional to the Reynolds' stress.

### 3. Signal Processing

As mentioned in the previous section, the components of  $\bar{V}$  and  $V'(t)$  (the mean and fluctuating components of velocity, respectively) individually satisfy equations (6.3) and (6.4). Since the detector produces only the absolute values of the frequencies, it is helpful to introduce the quantities

$$\begin{aligned}
 a &= (1 - \cos \theta) / \sin \theta , \\
 S_D &= \text{sign} (V_z - a V_r) , \\
 S_S &= \text{sign} (V_z + a V_r) , \\
 S_R &= S_D / S_S , \\
 C_z &= C S_D / 2 f_o \sin \theta .
 \end{aligned}$$

Then

$$(6.5) \quad \bar{V}_z = C_z \left( \frac{1}{S_R} \bar{f}_{d2} + \bar{f}_{d1} \right) ,$$

$$(6.6) \quad \bar{V}_r = a C_z \left( \frac{1}{S_R} \bar{f}_{d2} - \bar{f}_{d1} \right) ,$$

$$(6.7) \quad V'_z = C_z \left( \frac{1}{S_R} f_{d2} + f_{d1} \right) ,$$

$$(6.8) \quad V'_r = a C_z \left( \frac{1}{S_R} f_{d2} - f_{d1} \right) .$$

The mean frequencies  $\bar{f}_{d1}$  and  $\bar{f}_{d2}$  were read on frequency counters.

$\bar{V}_z$  was obtained by using these readings in equations (6.5) ( $\bar{V}_r$  was zero for this pipe flow).

The turbulence intensities are defined as the root-mean-square (RMS) values for the fluctuating velocities  $V'_z$  and  $V'_r$ , i.e.,  $[\overline{V'^2_z}]^{\frac{1}{2}}$  and  $[\overline{V'^2_r}]^{\frac{1}{2}}$ . These turbulence intensities are related to  $\text{RMS}_1$  and  $\text{RMS}_2$ , the meter readings of the RMS meters shown in Figure 6.2. In order to develop these relationships, consider the signal processing set-up of Figure 6.2.

The fluctuating D.C. voltage outputs from readout units 1 and 2,  $V'_1$  and  $V'_2$ , were amplified by amounts  $a_1$  and  $a_2$ , respectively. Both

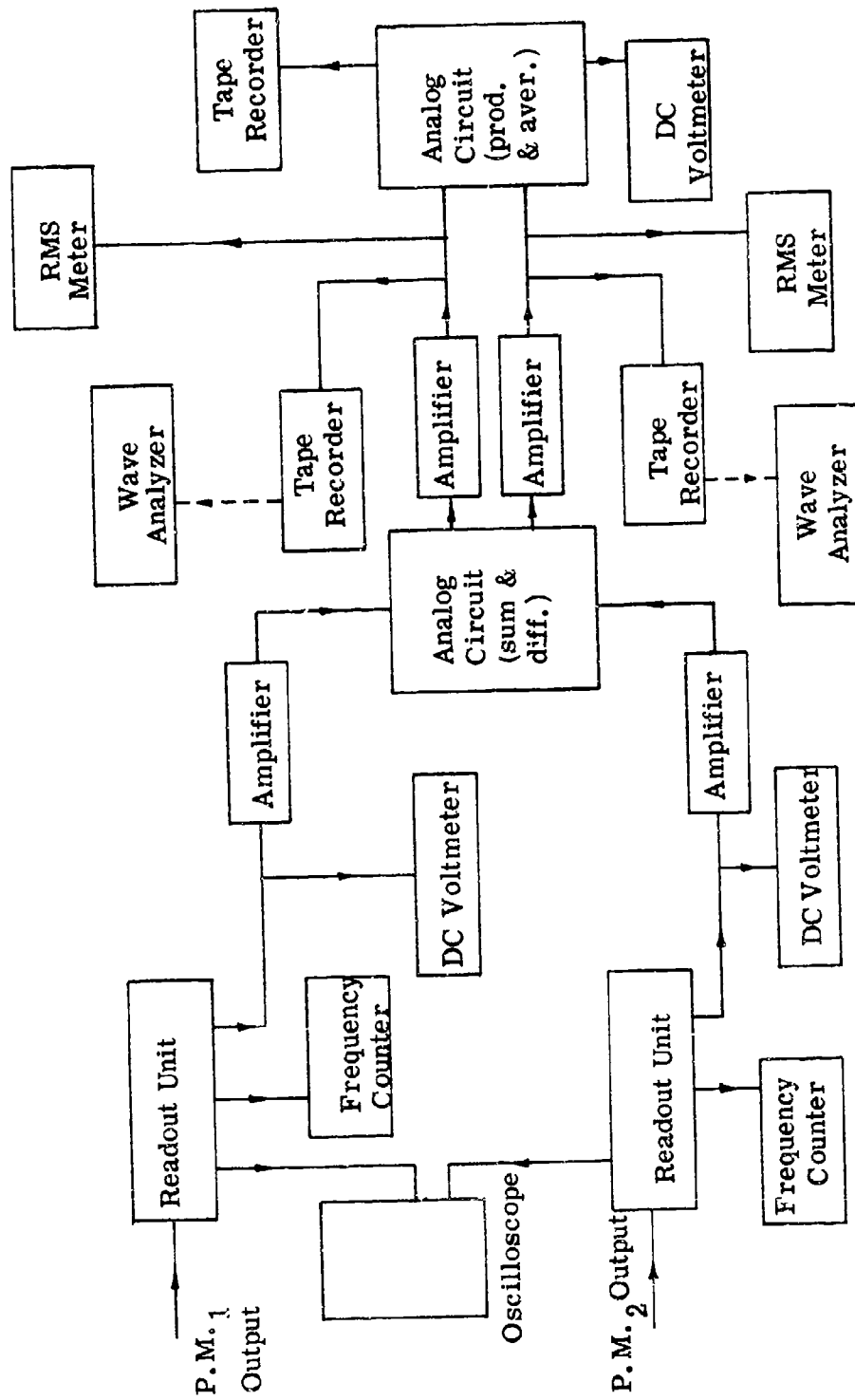


Figure 6.2  
Signal Processing Set-Up

signals were fed into the analog unit which yielded their difference and sum as outputs,

$$(6.9) \quad D = a_1 V'_1 - a_2 V'_2,$$

$$(6.10) \quad S = a_1 V'_1 + a_2 V'_2.$$

where  $D$  denotes the difference of the input voltages and  $S$  their sum.

Now  $a_1$  and  $a_2$  are chosen such that,

$$(6.11) \quad a_2 S_1 = a_1 S_2.$$

where  $S_1$  and  $S_2$  are the frequency-to-voltage sensitivities in megahertz per volt of readout units 1 and 2, respectively.

Multiplying equation (6.9) by  $S_1$

$$(6.12) \quad S_1 D = S_1 a_1 V'_1 - S_1 a_2 V'_2.$$

Using equation (6.11)

$$(6.13) \quad S_1 D = a_1 (S_1 V'_1) - a_1 (S_2 V'_2).$$

The fluctuating Doppler-shifted frequencies  $f'_{d1}$  and  $f'_{d2}$  are related to  $V'_1$  and  $V'_2$  by

$$(6.14) \quad f'_{d1} = S_1 V'_1,$$

$$(6.15) \quad f'_{d2} = S_2 V'_2.$$

Substituting equations (6.14) and (6.15) into equation (6.13)

$$S_1 D = a_1 (f'_{d1} - f'_{d2}).$$



$$(6.16) \quad f'_{d1} - f'_{d2} = \frac{S_1 D}{a_1} .$$

Substituting equation (6.16) into equation (6.7) for  $S_R = +1.0$ ,

$$(6.17) \quad V'_z = \frac{C_z S_1}{a_1} S .$$

Similarly

$$(6.18) \quad V'_r = \frac{C_z S_1}{a a_1} D .$$

Equations (6.17) and (6.18) define the relationship between the fluctuating components of velocity and the outputs of the sum and difference analog circuit.

The analog outputs D and S were further amplified by amounts  $b_1$  and  $b_2$ , respectively, before being fed into RMS meters whose readings were  $RMS_1$  and  $RMS_2$ .

$$(6.19) \quad RMS_1 = b_1 [\overline{D'^2}]^{\frac{1}{2}} ,$$

$$(6.20) \quad RMS_2 = b_2 [\overline{S'^2}]^{\frac{1}{2}} .$$

Therefore, from equation (6.17)

$$(6.21) \quad [\overline{V_z'^2}]^{\frac{1}{2}} = \frac{C_z S_1}{a_1 b_1} RMS_2 .$$

Likewise

$$(6.22) \quad [\overline{V_r'^2}]^{\frac{1}{2}} = \frac{C_z S_1}{a a_1 b_2} RMS_1 .$$

which relates the RMS meter readings to the turbulence intensities.

The Reynolds' stress is defined as  $\overline{V'_z V'_r}$ . Now, the output of the product and averaging analog circuit (PAAC) is related to the Reynolds' stress. The inputs to the PAAC were

$$(6.23) \quad b_1 S = \frac{b_1 a_1}{C_z S_1} V'_z ,$$

$$(6.24) \quad b_2 D = \frac{b_2 a_1 a}{C_z S_1} V'_r .$$

The output of the PAAC was

$$(6.25) \quad \text{PAAC} = \overline{b_1 S b_2 D}$$

$$(6.26) \quad \text{PAAC} = \frac{a a_1^2 b_1 b_2}{C_z^2 S_1^2} \overline{V'_z V'_r} .$$

Therefore,

$$(6.27) \quad \overline{V'_z V'_r} = \frac{C_z^2 S_1^2}{a_1^2 b_1 b_2 a} \text{PAAC} .$$

which relates the Reynolds' stress to the output of the PAAC.

The outputs of the sum and difference analog circuit  $\frac{b_1 a_1}{C_z S_1} V'_z$  and  $-\frac{b_2 a_1 a}{C_z S_1} V'_r$  were taped. They were subsequently each fed into the wave analyzer which yielded their power spectral densities

$$(6.28) \quad F_z(w) = k_z \int_{-\infty}^{\infty} e^{i w \tau} \overline{V'_z(t) V'_z(t + \tau)} d\tau ,$$

$$(6.29) \quad F_r(w) = k_r \int_{-\infty}^{\infty} e^{i w \tau} \overline{V'_r(t) V'_r(t + \tau)} d\tau .$$

which can be transformed into one-dimensional energy spectra in wave number space by using the transformation

$$(6.30) \quad k_1 = 2\pi w / \bar{V}_z ,$$

where  $k_1$  is the wave number. The wave analyzer was calibrated by lumping all of the calibration factors such as  $b_1$ ,  $a_1$ ,  $b_2$ , etc. into one parameter  $k$ . This parameter was determined by

$$(6.31) \quad \bar{V}_z^2 = 2 \int_0^\infty k_z F_z(w) dw ,$$

$$(6.32) \quad k_z = \frac{\bar{V}_z^2}{2 \int_0^\infty F_z(w) dw} .$$

Likewise

$$(6.33) \quad k_r = \frac{\bar{V}_r^2}{2 \int_0^\infty F_r(w) dw}$$

where  $\bar{V}_z^2$  and  $\bar{V}_r^2$  were known from previous measurements and the integrals were obtained as outputs on the wave analyzer.

## Chapter VII

### MEASUREMENTS AND OBSERVATIONS

#### 1. Discussion of the Turbulence Measuring Technique

The stated goals of this work were to measure the drag reduction, mean flow characteristics, and turbulence properties in the axial and radial directions for drag reducing pipe flows. To obtain such data with the beam configuration used in this work, one must generally process the signals from both optical units simultaneously, i.e., the readout unit outputs must be fed into the analog circuit (Figure 6.2) simultaneously. It is not possible to generate meaningful data by recording the output of one readout unit on tape, at a later time record the output of the other readout unit on tape, and to then read both tapes simultaneously into the analog circuit of Figure 6.2, for phase relationships would thereby be lost. Concern for this was occasioned because the Electronics, Inc. readout units used in this work have never been in working order at the same time. Thus it was never possible to process the data from channels 1 and 2 simultaneously. As a consequence it was not possible to measure the radial intensities or  $V'_z V'_r$  (unaveraged). What was done instead was to use the two-dimensional optical geometry to measure the Reynolds' stress and the mean velocity and to use a one-dimensional geometry (Chung and Graebel, (1972)) to measure  $V'_z$  and its spectra. This kept the loss of measurable data to a minimum.

All measurements were made at a Reynolds' number of 50,000 based on the average velocity in the pipe. Data for water was compared to that obtained for 50, 100, and 200 PPM solutions of Separan AP30 and water.

As mentioned before, the polymer injection technique used in this work is unique. It offers many advantages over the master batch technique commonly used in experimental work. As such, it is a promising technique for large-scale, accurate concentration polymer injection in laboratory or non-laboratory applications. It was expected that this injection technique would show significantly different drag reduction, mean flow, and turbulence properties than observed previously. That such was the case is shown in the following data.

## 2. Discussion of Results

### 2.1 Drag Reduction

Drag reduction was measured as a pressure loss by means of two side wall pressure taps located 11.875 feet apart. The pressure difference between them was measured on a U-tube manometer. In measuring the pressure loss of the polymer solutions, it was found that maximum drag reduction was established two minutes after the polymer injection pump was started. Therefore, all flow and turbulence measurements were made only after the pump had been operating for two minutes. Drag reduction effects were noted in the pipe for up to eight minutes after the pump was stopped. These time lags were due

to the presence of the mixing tank upstream of the pressure probes.

The percentage drag reduction was calculated by:

$$\text{Percentage Drag Reduction} = \frac{\Delta P_s - \Delta P_p}{\Delta P_s} \times 100$$

where:  $\Delta P_s$ : pressure loss due to friction, solvent only.

$\Delta P_p$ : pressure loss due to friction, polymer solution.

The percentage drag reduction, friction velocity  $V_T$ , the ratio of maximum to average velocity, and friction factor,  $f$ , for various polymer concentrations are presented in Table 7. 1. The friction factors of this work are compared to those of Chung and Graebel (1972), for the same polymer, polymer concentration, and Reynolds' number. Whereas the friction factor for water was found to be slightly lower in this work, the friction factors for the polymer solutions are higher than found by Chung and Graebel (1972). This indicates that less drag reduction has occurred in the present study. One reason for this might be that the polymer powder was not completely dissolved and therefore the actual polymer concentration was less. Since drag reduction increases with increased polymer concentration, up to a limit (Virk, Mickley, and Smith, 1970), this would explain the lower drag reduction observed. Solid, undissolved polymer particles were, in fact, observed passing through the test section.

The ratio of maximum to average velocities were higher for all of the polymer concentrations than for water. This contradicts the findings of Chung and Graebel (1972) and Seyer and Metzner (1969). The reason

Table 7.1

## DRAG REDUCTION PARAMETERS

Polymer Concentration	Percentage Drag Reduction	$V_{\tau}$ (ft/sec)	$\frac{\bar{V}_{\max}}{\bar{V}_{av}}$	$f$	$f$ Chung and Graebel (1972)
0	----	0.146	1.17	0.0171	0.020
50	26.9	0.126	1.18	0.0125	----
100	35.8	0.118	1.22	0.0110	0.007
200	42.8	0.111	1.29	0.0098	0.006

for this is that the presence of the solid, undissolved polymer particles significantly effected the mean flow and turbulence properties of this pipe flow. Subsequent data will bear this out.

## 2.2 Mean Velocity Profiles

The axial mean velocity profiles for water, 50, 100, and 200 PPM solutions of Separan AP30 flowing at a Reynolds' number of 50,000 are plotted in Figure 7.1. The mean velocities have been normalized by the maximum velocity, i.e., the centerline velocity. The abscissa is the normalized distance from the wall,  $\bar{r} = 1 - \frac{r}{a}$ , where  $\bar{r}$  is the distance from the flow axis and  $a$  the radius of the pipe. The confidence band of this data is 5 per cent. The mean velocity profile of Sandborn (1955), who measured air flow in a pipe at a Reynolds' number of 50,000 is also shown in Figure 7.1. His results are seen to be in general agreement with those of the present work. It is seen from Figure 7.1 that the velocity profiles tend to become less blunt as the polymer concentration increases. This is in direct contradiction with the work of Chung and Graebel (1972) and Rudd (1972) who show flatter velocity profiles for polymer solutions than for water. Both studies were done using the same polymer and similar polymer concentrations at the same Reynolds' number. This apparent anomaly is just a manifestation of the particulate nature of the flow. Daily and Hardison (1964) found that the velocity profile for a 2.0% (by volume) concentration of spherical plastic particles, 0.004 to 0.006 inches in diameter, in a 100,000 Reynolds' number flow was



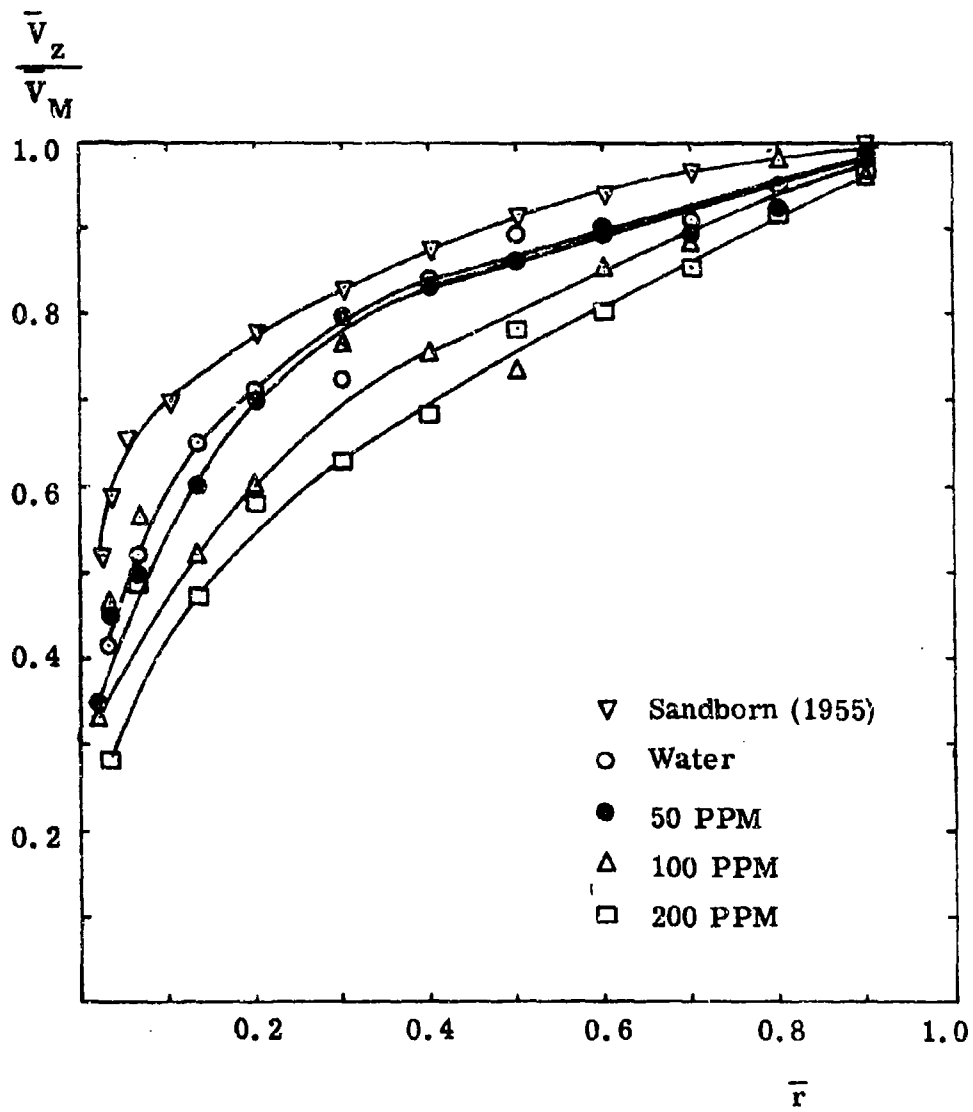


Figure 7.1

Axial Mean Velocity Profiles at  $Re = 5(10)^4$

much less blunt than for a purely water flow. Furthermore, they found that the ratio of maximum to average velocity for the particulate flow was higher than for the water flow. This correlates with what was observed in the present work. It is reasonable to conclude that, for the core region, the mean flow characteristics of the polymer solution are dominated by particulate effects.

### 2.3 Turbulence Intensities

The axial turbulence intensity profiles are shown in Figure 7.2. The intensities have been normalized with respect to the maximum mean velocities. As mentioned before, the intensity profiles were measured using a one-dimensional set-up similar to the one used in the work of Chung and Graebel (1972). The transformation from the two-dimensional to one-dimensional set-up was accomplished by simply replacing B. S. <sub>2</sub> with a mirror. It was hoped that an included beam angle (the angle between the incident and reference beams) of 20 degrees could be used, allowing for a greater instrument sensitivity. This was not possible, however, since the heterodyned signal at this angle was too weak and broadened to yield meaningful data. The weakness of the signal was due to the low forward scattering intensity at this relatively large included beam angle. (Forward scattering intensity decreases rapidly with increasing included beam angle.) The signal broadening was due to the large measuring volume, also a consequence of the large angle (Jackson and Paul, 1970). Experience has shown that the optimal

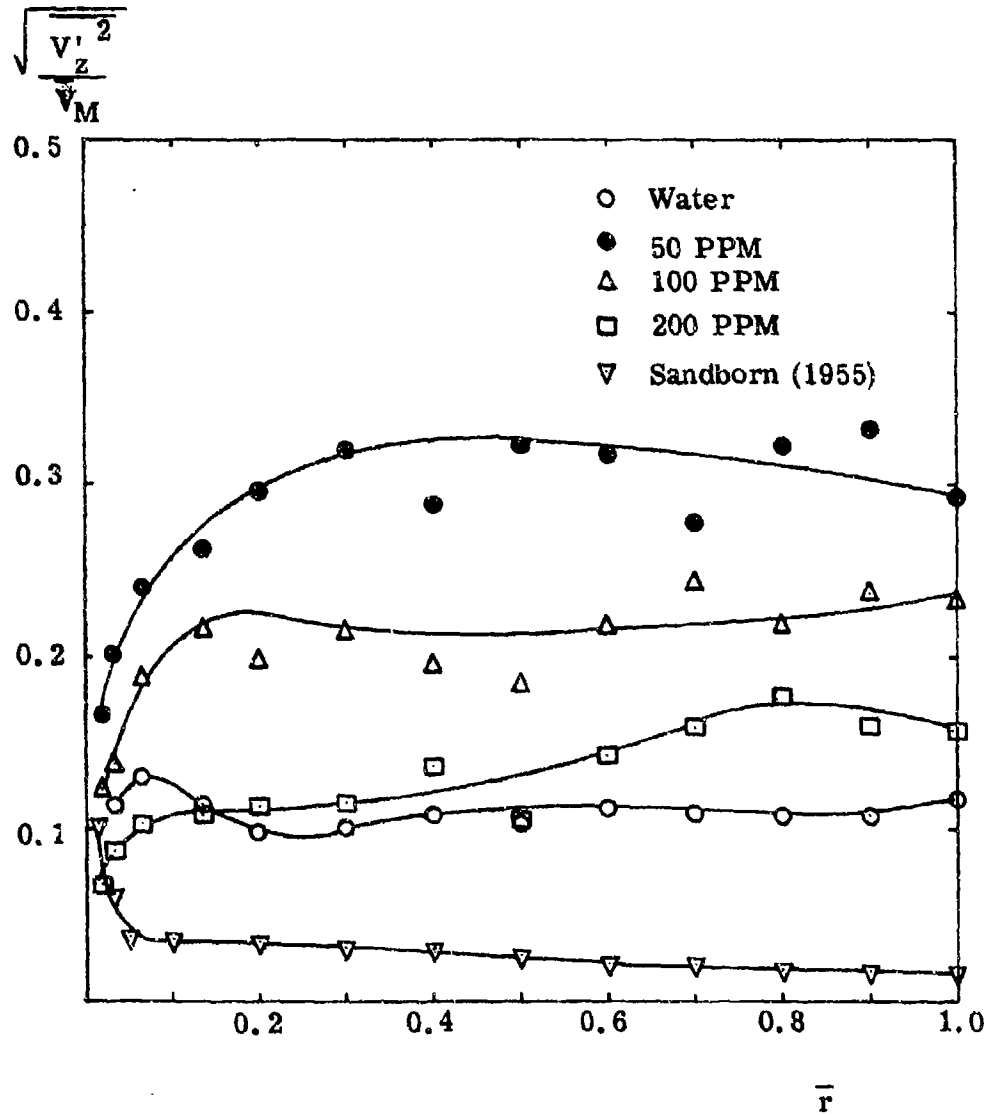


Figure 7.2

Axial Turbulence Intensities at  $Re = 5(10)^4$

included beam angle is approximately 12 degrees for this set-up. Thus, when the beam angle was decreased to 12.4 degrees, a clear heterodyned signal was observed.

Referring to Figure 7.2, it is seen that the axial turbulence intensities are everywhere higher for the polymer solutions than for water. However, others have found that the axial intensities are lower for polymer solutions than for water in the range  $0.4 < \bar{r} < 1.0$  and higher in the range  $0 < \bar{r} < 0.4$  (Chung and Graebel, 1972) and (Rudd, 1972). That the intensities are higher for the polymer solutions in the region  $0.4 < \bar{r} < 1.0$  in this work is a consequence of the particulate nature of the flow in the core region. The particles in the flow generate eddies which are manifested as higher turbulence intensities. This was found experimentally by Daily and Hardison (1964) who noted higher axial intensities for a particulate flow than for water, in a pipe flow. The intensities of Figure 7.2 show a marked decrease, all across the profile, with increasing polymer concentration. Thus, the trend of the polymer intensities is toward the usually observed drag reducing polymer effect. This would seem to indicate that the effect of the increase of polymer concentration is stronger than the effect of the increase in particle concentration. It would seem that at some higher polymer concentration than measured, the polymeric action would dominate the particulate effect to the extent of showing the usually observed turbulence properties of drag reducing flows. Subsequent Reynolds' stress and energy spectra data supports this hypothesis.

## 2.4 Reynolds' Stress

The normalized Reynolds' stress,  $\overline{V'_z V'_r} / \bar{V}_{\max}^2$ , is shown in Figure 7.3 plotted against  $\bar{r}$ . The Reynolds' stress can be thought of as a measure of the rate of transport of z-momentum through a surface normal to the r-axis by the turbulent fluctuations. It may also be thought of as an additional stress due to the presence of turbulent velocity fluctuations. In light of this, it would be expected, that for a particulate flow (at least in the core region) the Reynolds' stress would be higher than for the solvent flow. That the Reynolds' stress for the polymer solutions are higher than for water reiterates the particulate nature of the polymer flow.

The turbulent energy equation for fully developed, incompressible, axially symmetric flow is:

$$(7.6) \quad \overline{V'_z V'_r} \frac{d\bar{V}_z}{dr} + \frac{1}{r} \frac{d}{dr} r V'_r \left[ \frac{V'^2_z + V'^2_r + V'^2_\theta}{2} + \frac{p}{\rho} \right] \\ - \frac{V}{r} \frac{d}{dr} r \frac{d}{dr} \left[ \frac{V'^2_r + V'^2_z + V'^2_\theta}{2} \right] + V \left( \frac{\partial \overline{V'_i}}{\partial x_j} \right) \left( \frac{\partial \overline{V'_i}}{\partial x_j} \right) = 0,$$

where the term  $\overline{V'_z V'_r} \frac{d\bar{V}_z}{dr}$

represents a net rate of exchange of energy between the mean flow and the turbulent field through the working of the Reynolds' stress against the mean velocity gradient. In other words, it represents the production of turbulent energy. It has been postulated (Walsh, 1967) that the small

$$\overline{V'_z V'_r} / \bar{V}_M^2$$

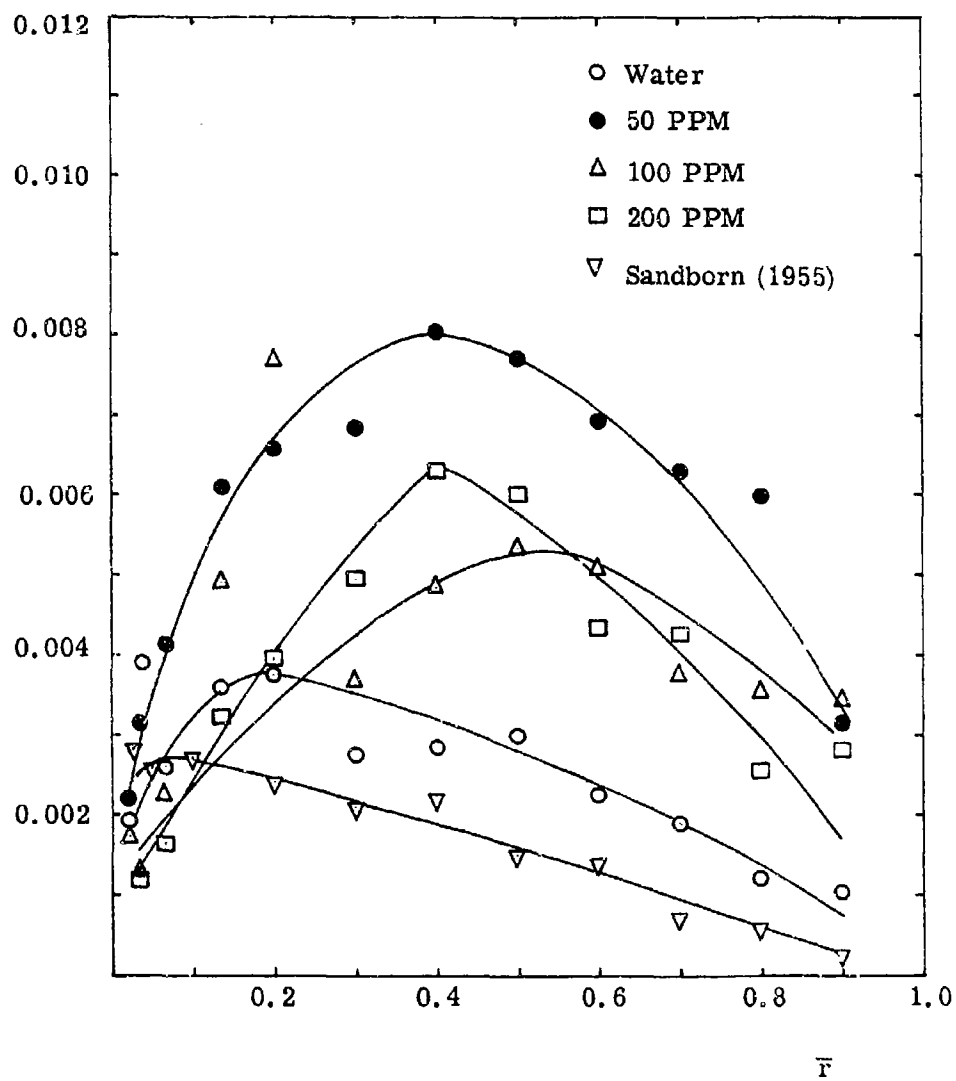


Figure 7.3

Reynolds' Stress at  $Re = 5(10)^4$

eddies near the wall which grow and form the large-scale turbulence, gain energy through interaction with the mean velocity profile through its' Reynolds' stress and lose energy by viscous dissipation and local storage in the polymer molecules. If the eddies gain more energy than they lose, they tend to grow. If they lose more energy than they gain, they will be annihilated by viscous dissipation. The effect of the polymer is to inhibit growth of these eddies and to facilitate their destruction through the action of viscosity. Thus, there will be fewer small scale eddies per unit volume per unit time and as a consequence, less large scale turbulence. This, Walsh feels, is the mechanism for drag reduction. In light of this theory, it would be expected that the production term should be less for the polymer solution than for the solvent, at least near the wall. Referring to Figure 7.1 and 7.3, it is seen that  $\overline{V_z'V_r'} \frac{d\bar{V}_z}{dr}$  is less for the 200 PPM polymer solution than for water in the region near the wall. This would seem to indicate that, for the 200 PPM solution, the polymeric action is dominating the particulate effect in the turbulent properties.

## 2.5 Energy Spectra

One-dimensional energy spectra are plotted versus one-dimensional wave number space in Figures 7.4, 7.5, and 7.6 for various polymer concentrations at three radial locations;  $\bar{r} = 1.00, 0.500, \text{ and } 0.020$ , respectively. These spectra were obtained by tape recording the axial velocity fluctuations (the bandwidth of the tape recorder being D. C. to

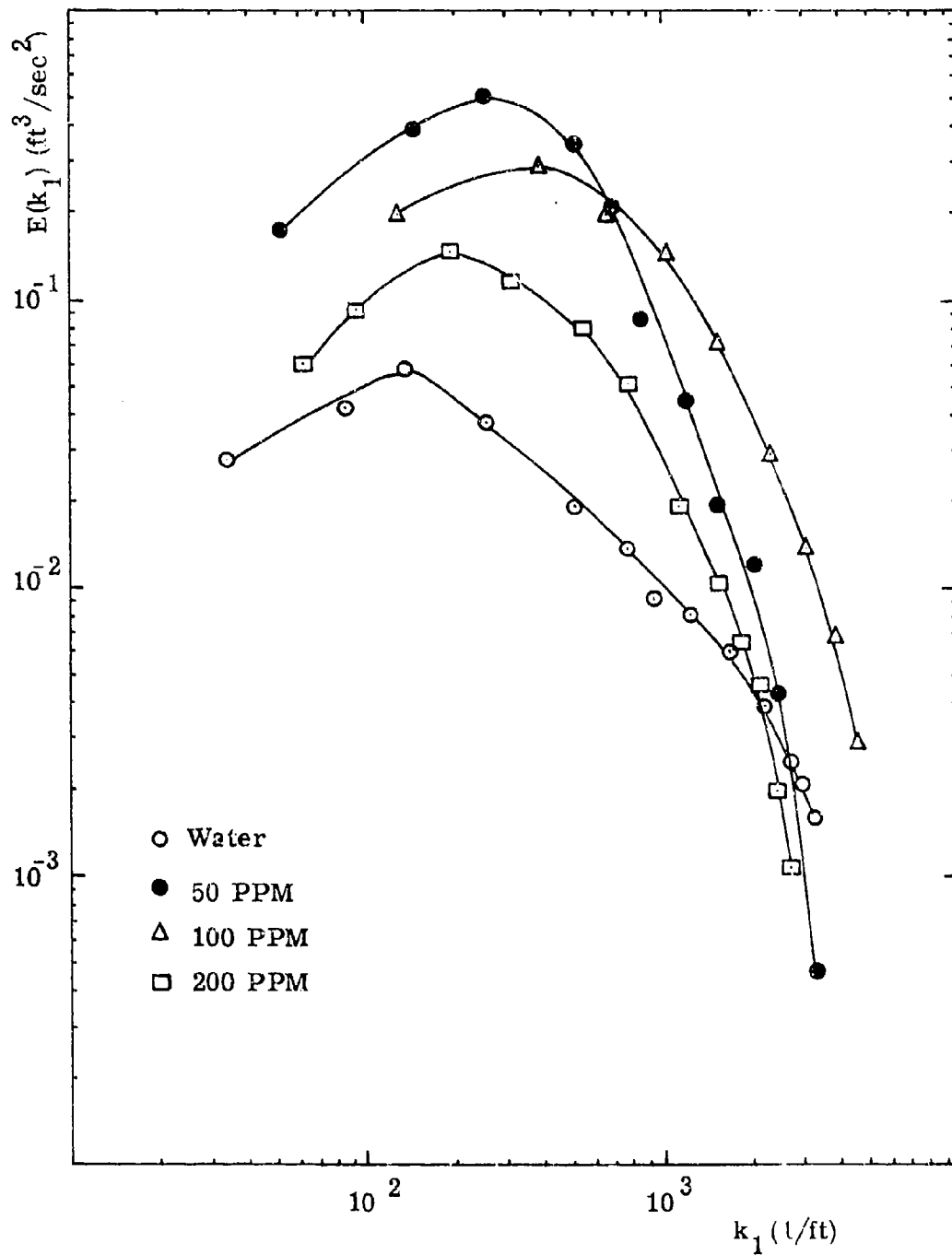


Figure 7.4

$V'_z$  Energy Spectra at  $\bar{r}=1.00$  at  $Re = 5(10)^4$



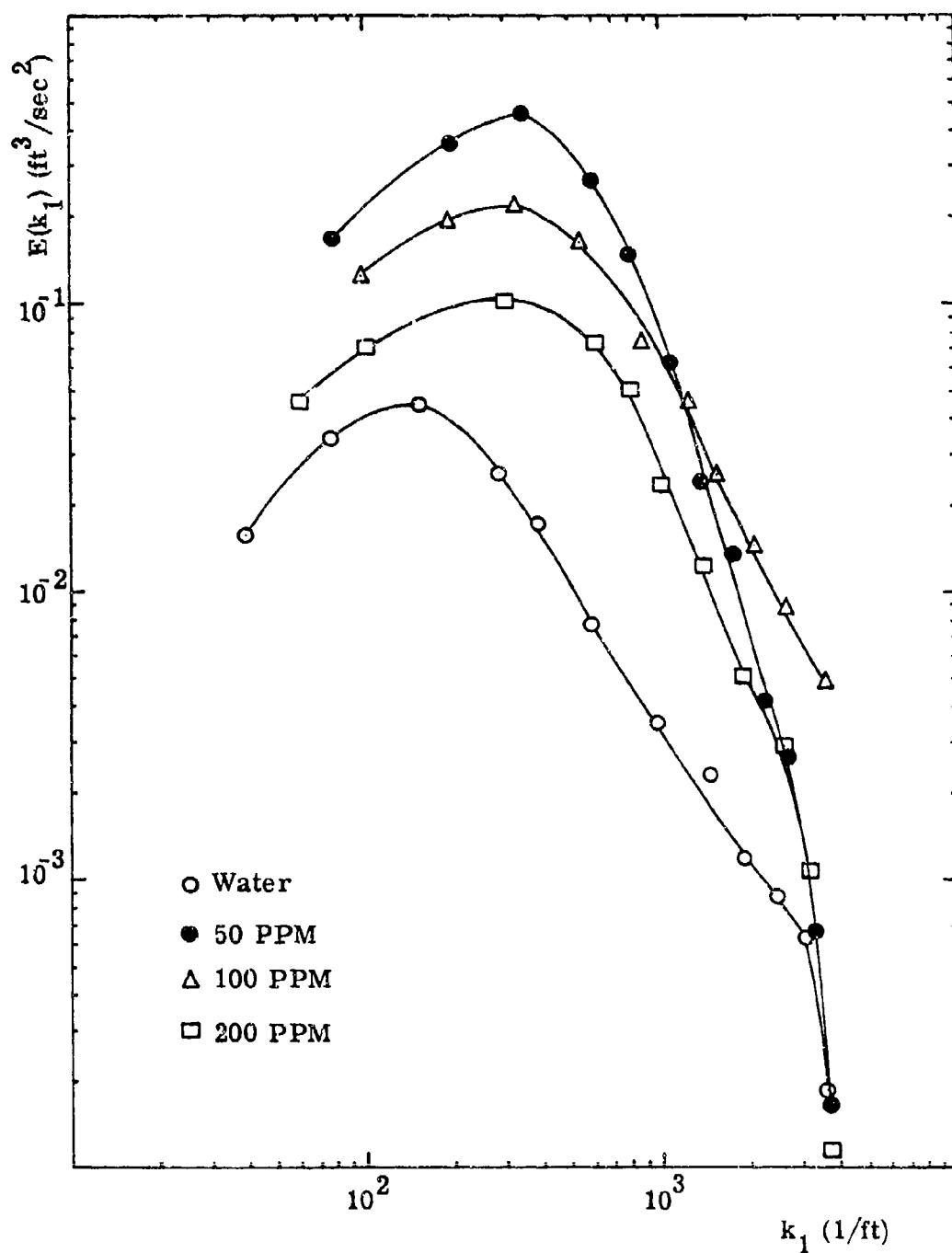


Figure 7.5

$V'_z$  Energy Spectra at  $\bar{r} = 0.500$  at  $Re = 5(10)^4$

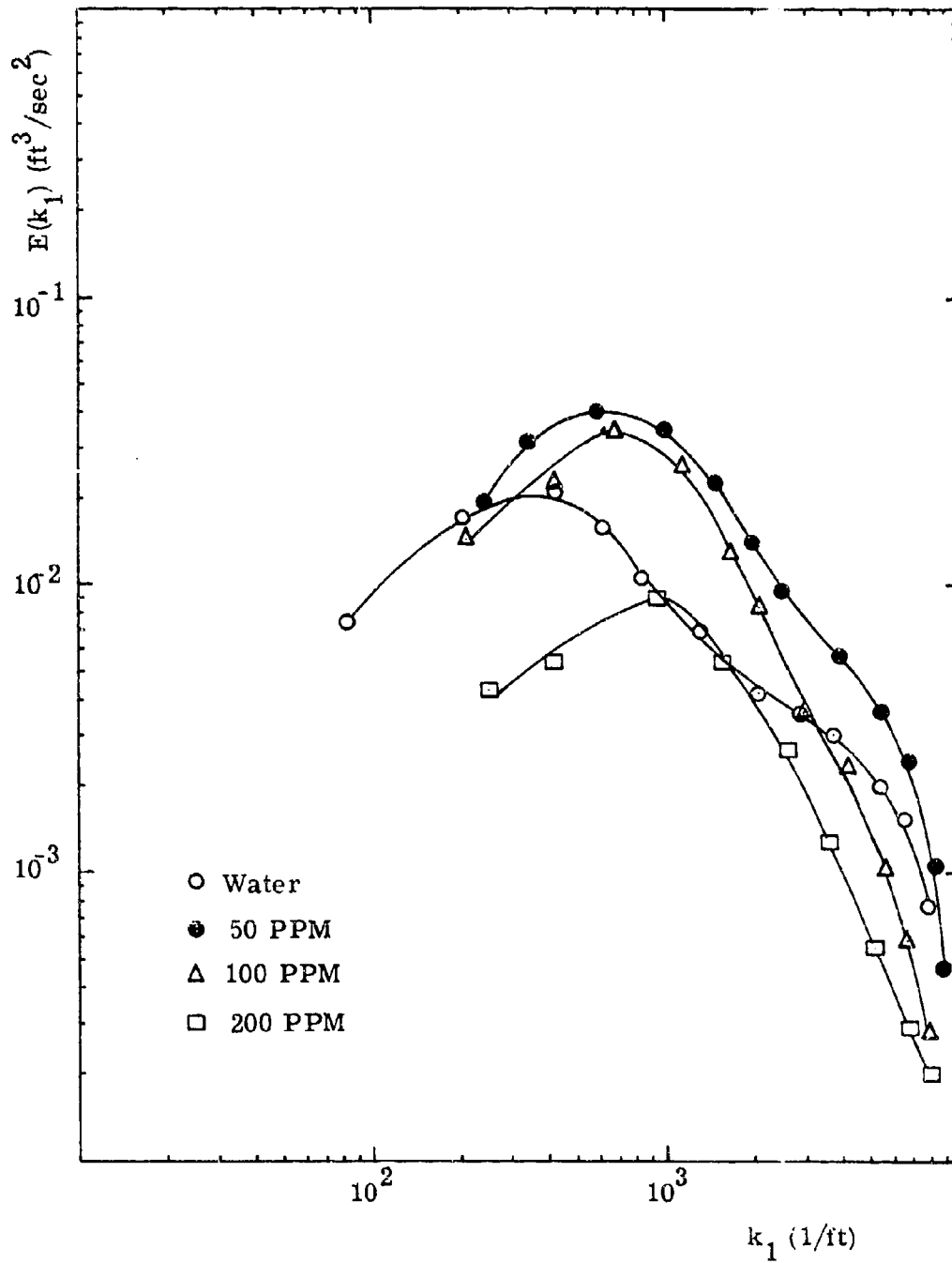


Figure 7.6

$V'_Z$  Energy Spectra at  $\bar{r} = 0.020$  Except for Water at  $\bar{r} = 0.32$  at  $Re \ 5(10)^4$

2500 Hz) and later reading this taped data into a wave analyzer. The data was analyzed at a 13 Hz sec sweep rate using a filter whose effective bandwidth was 13 Hz. The sample time was 180 seconds. Thus, the expected error is about 2%.

There are no valid conclusive energy spectra of polymer flows. Of the few investigators who have attempted energy spectra, the validity of the work of Virk et al (1967), Wells, Harkness and Meyer (1968), and Johnson and Barchi (1968) must be seriously questioned due to the basic measuring techniques that they employed. (This was discussed in detail in Chapter 1). The energy spectra of Chang and Graebel (1972), who used a LDA in their work, are inconclusive as they show no general trend. Others who have studied drag reducing flows with laser anemometers have not reported energy spectra because they processed their P.M. outputs with spectrum analyzers. Thus, the time domain is annihilated and there can be no transformation to the frequency or wave number domain required to produce energy spectra.

Referring to Figures 7.4, 7.5, and 7.6, it is seen that the polymer spectra are generally higher in the low wave number (energy containing) range at all radial positions than the water spectra. As it would be expected that a particulate flow would be more energetic than a solvent flow, this is another reflection of the particulate nature of the polymer flows. However, the energy spectra decrease with increasing polymer concentration in this wave number range. Since it is expected that polymeric action lowers the energy spectra profile, this again shows

the dominance of the polymeric effect over the particulate effect. The spectra do not generally exhibit the  $-5/3$  slope predicted by Kolomogoroff's hypothesis. This is not surprising since the Reynolds' number for these flows was only 50,000 and therefore probably not high enough to satisfy the conditions of this hypothesis (Hinze, 1959). Of special interest are the spectra at  $\bar{r}=0.020$  (Figure 7.6) which is near the wall. It is seen that spectra for the 100 and 200 PPM concentrations are less in the high wave number (the dissipative) range than the water spectra. This confirms Walshs' theory that there are fewer small eddies per unit volume per unit time in polymer flows than in water flows. Furthermore, the spectra of the 200 PPM solution is everywhere less than the water curve, showing the complete dominance of the polymeric action in the wall region at this concentration.

### 3. Summary and Conclusions

The drag reduction, mean flow, and turbulence properties of drag reducing flows were measured using a two-dimensional laser anemometer technique.

The optical bench used was designed to offer experimental flexibility and ease of alignment as well as to satisfy the spatial requirements of photomixing and to minimize spectral broadening inherent in the optical set-up. The signal-to-noise ratio of the optical set-up and the photomultiplier tube was studied and the system was operated in order to maximize this ratio.

A flow-through system was chosen for this work to minimize the effects of polymer degradation. The polymer injection system was unique to laboratory work. The polymer powder was injected directly into the water flow as a slurry of polymer and methanol. This technique was used to prevent both polymer aging and the tedium associated with the commonly used master-batch technique.

The key to the signal processing set-up is the readout unit which takes the P. M. signal and processes it to yield the mean velocity and a D. C. signal directly proportional to the fluctuating component of velocity. Two of these units operating simultaneously with a two-dimensional LDA allow signal processing to be accomplished with the same equipment used to process signals from X-wires in hot-wire anemometry. Unfortunately, the readout units have not reached the stage of development where they are completely reliable. In fact, the two units used in this work were never both in operating order simultaneously. Thus, it was not possible to make all of the measurements potentially possible with a two-dimensional LDA.

The data generally contradict the work of previous investigators. The percentage drag reduction for 50, 100, and 200 PPM solutions of Separan AP30 and water is lower than that found previously. This is the first clue that the polymer powder injected did not dissolve completely. The mean velocity profiles were less blunt and the ratio of maximum to average velocities were higher for the polymer solutions

than for water. This disagrees with previous work and is an indication of the particulate (undissolved polymer powder) nature of the flow. The turbulence intensities and Reynolds' stresses are higher for the polymer solutions than for water, at least in the core region. This also is not what would be expected for the usual drag reducing flow but rather for a particulate flow. The higher energy spectra observed for the polymer solutions than for the water in the energy (low) wave number range is another indication of the essentially particulate nature of the polymer flows.

Thus the data shows that, for low polymer concentrations, using this polymer injection technique, the flow is dominated by particulate effects. As polymer concentration increases, however, polymeric effects are seen to dominate the particulate effects to the extent that at the 200 PPM concentrations the usual drag reduction phenomena begins to appear in the turbulence properties. This is especially noticable in the wall region where polymeric action is the strongest.

## REFERENCES

- Adrian, R. J. and Goldstein, R. J. 1971. Analysis of a Laser-Doppler Anemometer. J. Phys. E (Sci. Instrum.) 4: 505-11.
- Arunachalam, Vr. and Fulford, G. D. 1971. Adsorption Measurements in Dilute Solutions of a Drag-Reducing Polymer. Chem. Eng. Sci. 26: 1065-73.
- Astarita, G. and Nicodemo, L. 1966. Velocity Distributions and Normal Stresses in Viscoelastic Turbulent Pipe Flow. AIChE J. 12: 478-83.
- Bedi, P. S. 1971. A Simplified Optical Arrangement for the Laser Doppler Velocimeter. J. Phys. E (Sci. Instrum.) 4: 27-8.
- Born, M. and Wolf, E. 1964. Principles of Optics. London: Pergamon Press.
- Chu, B. and Schoernes, F. J. 1968. The Laser-Homodyne "Self-Beating" Technique in Light Scattering. J. Colloid Interface Sci. 27: 424-31.
- Chung, J. S. and Graebel, W. P. 1972. Laser Anemometer Measurements of Turbulence in Non-Newtonian Pipe Flows. Phys. Fluids 15: 546-554.
- Daily, J. W. and Hardison, R. L. 1964. Rigid Particle Suspensions in Turbulent Shear Flow: Measurement of Total Head, Velocity and Turbulence with Impact Tubes. Hyd. Lab. Rep; Dept. of C. E.; M.I.T. 67: 1-73.
- Denison, E. B., Stevenson, W. H. and Fox, R. W. 1971. Laminar Flow Measurements with a Directionally Sensitive Laser Velocimeter. AIChE J. 17: 781-7.
- Durst, F. and Whitelaw, J. H. 1971. Integrated Optical Units for Laser Anemometry. J. Phys. E (Sci. Instrum.) 4: 804-8.
- Elata, C., Lehrer, J. and Kahanovitz, A. 1966. Turbulent Shear Flow of Polymer Solutions. Isr. J. Technol. 4: 87-95.
- El'perin, I. T., Smol'skii, B. M. and Leventhal, L. I. 1967. Decreasing Hydraulic Resistance in Pipelines. Int. Chem. Eng. 7: 276-8.
- Foreman, J. W., George, E. W., Jetton, J. L., Lewis, R. D., Thornton, J. R. and Watson, H. J. 1966. Fluid Flow Measurements with a Laser-Doppler Velocimeter. IEEE J. Quantum Electron. QE-2: 260-6.

- Foreman, J. W., George, E. W., and Lewis, R. D. 1965. Measurement of Localized Flow Velocities in Gases with a Laser-Doppler Flowmeter. Appl. Phys. Lett. 7: 77-8.
- Fridman, J. D., Kinnard, K. F., and Meister, K. 1969. Laser Doppler Instrumentation for the Measurement of Turbulence in Gas and Fluid Flows. New York: Electro-Opt. Sys. Des. Conf.
- Fridman, J. D., Meister, K. A., and Young, R. M. 1971. Wide Band Frequency Trackers in Laser Doppler Velocimeter Systems. Las Vegas: Seventeenth Nat. Instr. Symp; Ind. Soc. Am.
- Gadd, G. 1968. Differences in Normal Stress in Aqueous Solutions of Turbulent Drag-Reducing Additives. Nature. 212: 1348-52.
- Goldstein, R. J., Adrian, R. J., and Kreid, D. K. 1969. Turbulent and Transition Pipe Flow of Dilute Aqueous Polymer Solutions. Ind. and Eng. Chem., Fund A.M. 8: 498-502.
- Goldstein, R. J. and Kreid, D. K. 1967. Measurement of Laminar Flow Development in a Square Duct Using a Laser-Doppler Flowmeter. J. Appl. Mech., Trans. ASME. 67-APM-37.
- Greated, C. 1970. Measurement of Reynolds' Stresses Using Improved Laser Flow Meter. J. Sci. Instrum. 3: 753-8.
- Greated, C. A. 1971. Resolution and Back Scattering Optical Geometry of Laser Doppler Systems. J. Phys. E. (Sci. Instrum.) 4: 585-8.
- Greated, C. and Durrant, T. S. 1971. Signal Analysis for Laser Doppler Measurements. J. Phys. E. (Sci. Instrum.) 4: 24-6.
- Hinze, J. O. 1959. Turbulence. New York: McGraw-Hill.
- Hoyt, J. W. 1972. The Effect of Additives on Fluid Friction. J. Basic Eng., Trans. ASME. 94: 258-85.
- Hoyt, J. W. and Fabula, A. G. 1964. The Effect of Additives on Fluid Friction. Proc. Fifth Symp. on Nav. Hydraulics. 947.
- Huifaker, R. M. 1970. Laser Doppler Detection Systems for Gas Velocity Measurements. Appl. Opt. 9: 1026-39.
- Jackson, D. A. and Paul, D. M. 1971. Measurement of Supersonic Velocity and Turbulence by Laser Anemometry. J. Phys. E. (Sci. Instrum.) 4: 173-7.



- Johnson, B. and Barchi, R. H. 1968. Effect of Drag-Reducing Additives on Boundary-Layer Turbulence. J. Hydronautics, 2: 168-75.
- Kalashnikow, V. N. and Kudin, A. M. 1969. Karman Vortices in Flows of Solutions of Friction-Drag-Reducing Polymers. Izy. Akad. Nauk. SSSR Mekh. Zh. Gaz. 4: 184-8.
- Lanz, O., Johnson, C. C., and Morikawa, S. 1970. High-Resolution Laser Doppler Velocity Measurements of Bidirectional Pulsatile Flow. Appl. Phys. Lett. 17: 523-5.
- Latto, B. and Shen, C. H. 1970. Effect of Dilute Polymer Solution Injection on External Boundary-Layer Phenomena. Can. J. Chem. Eng. 48: 34-8.
- Laufer, J. 1953. The Structure of Turbulence in Fully Developed Pipe Flow. NACA TN. 2954: 1-53.
- Lumley, J. L. 1964. Turbulence in Non-Newtonian Fluids. Phys. Fluids. 8: 335-7.
- Lumley, J. L. 1969. Drag Reduction by Additives. Ann. Rev. Fluid Mech. 1: 367-83.
- Mezumder, M. K. and Wankum, D. L. 1970. SNR and Spectral Broadening in Turbulence Structure Measurement Using a cw Laser. Appl. Opt. 9: 633-7.
- Metzner, A. B. and Astarita, G. 1967. External Flows of Viscoelastic Materials; Fluid Property Restrictions on the Use of Velocity-Sensitive Probes. AIChE J. 13: 550-5.
- Metzner, A. B. and Park, M. G. 1964. Turbulent Flow Characteristics of Viscoelastic Fluids. J. Fluid Mech. 20: 293-303.
- Meyer, W. A. 1966. Correlation of the Frictional Characteristics for Turbulent Flow of Dilute Viscoelastic Non-Newtonian Fluids in Pipes. AIChE J. 12: 522-5.
- Morton, J. B. and Clark, W. H. 1971. Measurement of Two-Point Velocity Correlations in a Pipe Using Laser Anemometers. J. Phys. E. (Sci. Instrum.) 4: 809-14.
- Nicedemo, L., Acierno, D., and Astarita, G. 1969. Velocity Profiles in Turbulent Pipe Flow of Drag-Reducing Liquids. Chem. Eng. Sci. 24: 1241-6.

- Oldroyd, J. G. 1948. A Suggested Method of Detecting Wall Effects in Turbulent Flow Through Pipes. Proc. of First Inter. Rheo. Cong. II-130-134.
- Patterson, G. K., Zankin, J. L., and Rodriguez, J. M. 1969. Drag Reduction. Polymer Solutions, Soap Solutions, and Solid Particle Suspensions in Pipe Flow. Ind. and Eng. Chem., Fundam. 61: 22-30.
- Peterlin, A. 1970. Molecular Model of Drag Reduction by Polymer Solutes. Nature. 227: 598-9.
- Rodriguez, J. M., Patterson, G. K., and Zankin, J. L. 1971. Measurement of Turbulence Intensities with Piezoelectric Probes in Viscoelastic Fluids. J. Hydronautics. 5: 101-6.
- Rolfe, E., Silk, J. K., Booth, S., Meister, K., and Young, R. M. 1968. Laser Doppler Velocity Instruments. NASA CR. 1199.
- Ruckenstein, E. 1971. On the Mechanism of Drag Reduction in Turbulent Flow of Viscoelastic Liquids. Chem. Eng. Sci. 26: 1075-9.
- Rudd, M. J. 1969. Measurements Made on a Drag Reducing Solution with a Laser Velocimeter. Nature. 224: 587-8.
- Rudd, M. J. 1972. Velocity Measurements Made with a Laser Dopplermeter on the Turbulent Pipe Flow of a Dilute Polymer Solution. J. Fluid Mech. 51: 673-85.
- Sandborn, V. A., 1955. Experimental Evaluation of Momentum Terms in Turbulent Pipe Flow. NACA TN. 3226: 1-40.
- Seyer, F. A. and Metzner, A. B. 1969. Turbulence Phenomena in Drag Reducing Systems. AIChE J. 15: 426-34.
- Smith, K. A., Merrill, E. W., Mickley, H. S., and Virk, P. S. 1967. Anomalous Pitot Tube and Hot-Film Measurements in Dilute Polymer Solutions. Chem. Eng. Sci. 4: 619-26.
- Stevenson, W. H. 1970. Analysis of Rotating Radial Diffraction Gratings. Appl. Opt. 9: 649-53.
- Toms, B. A. 1948. Some Observations on the Flow of Polymer Solutions Through Straight Tubes at Large Reynolds Numbers. Proc. of First Inter. Rheo. Cong. II-135-41.

- Virk, P. S. 1971a. Drag Reduction in Rough Pipes. J. Fluid Mech. 45: 225-46.
- Virk, P. S. 1971b. An Elastic Sublayer for Drag Reduction by Dilute Solutions of Linear Macro-molecules. J. Fluid Mech. 45: 417-40.
- Virk, P. S., Merrill, E. W., Mickley, H. S., Smith, K. A., and Mollo-Christiansen, E. L. 1967. The Toms Phenomenon; Turbulent Pipe Flow of Dilute Polymer Solutions. J. Fluid Mech. 30: 305-28.
- Virk, P. S., Mickley, H. S., and Smith, K. A. 1970. Ultimate Asymptote and Mean Flow Structure of Tom's Phenomenon. J. Appl. Mech., Trans. ASME. 37: 488-93.
- Walsh, M. 1967. Theory of Drag Reduction in Dilute High-Polymer Flows. Int. Shipbldg. Progr. 14: 134-9.
- Walters, R. R. and Wells, C. S. 1971. An Experimental Study of Turbulent Diffusion of Drag-Reducing Polymer Additives. J. Hydronautics. 5: 65-72.
- Watson, Jr., R. C., Lewis, R. D. and Watson, H. J. 1969. Instruments for Motion Measuring Using Laser Doppler Heterodyning Techniques. ISA Trans. 8: 20-8.
- Wells, C. S., Harkness, J., and Meyer, W. A. 1968. Turbulence Measurements in Pipe Flow of Drag-Reducing Non-Newtonian Fluid. AIAA J. 6: 250-7.
- Wilmschurst, T. H. 1971. Resolution of the Laser Fluid-Flow Velocimeter. J. Phys. E. (Sci. Instrum.) 4: 77-80.
- Wilmschurst, T. H., Greated, C. A., and Manning, R. 1971. A Laser Fluid-Flow Velocimeter of Wide Dynamic Range. J. Phys. E. (Sci. Instrum.) 4: 81-5.
- Woods, M. E., Dodge, J. S., and Krieger, I. M. 1968. Emulsion Polymerization with Mixtures of Anionic and Nonionic Surfactants. J. Paint Technol. 40: 541-8.
- Yeh, Y. and Cummins, H. Z. 1964. Localized Fluid Flow Measurements with an He-Ne Laser Spectrometer. Appl. Phys. Lett. 4: 176-8.

## Appendix A

### REFRACTIVE EFFECT OF TEST SECTION AND WATER ON BEAM GEOMETRY OF A TWO-COMPONENT LASER-DOPPLER ANEMOMETER

The velocity to frequency relationship was shown in Chapter II to be

$$(A.1) \quad V_z = \frac{\lambda_\theta (f_{d2} - f_{d1})}{2 \sin \theta} ,$$

and

$$(A.2) \quad V_r = \frac{\lambda_\theta (f_{d2} + f_{d1})}{2(1 - \cos \theta)} .$$

where  $\lambda_\theta$  is the wavelength of the incident light in the fluid flow and  $\theta$  is the angle of incidence in the fluid flow. Due to the refractive properties of the test section and the water flow, this  $\lambda_\theta$  will be different than its value in air. Likewise the angle of incidence,  $\theta$ , will be different than the angular position,  $\phi$ , (see Figure A.1) of the reference beams before they hit the test section.

The relationship between  $\theta$  and  $\phi$  can be found by considering Figure A.1 and Snell's law:

$$(A.3) \quad \frac{\sin \theta}{n_\theta} = \frac{\sin \phi}{n_\phi} ,$$

where  $n$  is the index of refraction.

Thus

$$(A.4) \quad \theta = \sin^{-1} \left[ \frac{n_\theta}{n_\phi} \sin \phi \right] .$$

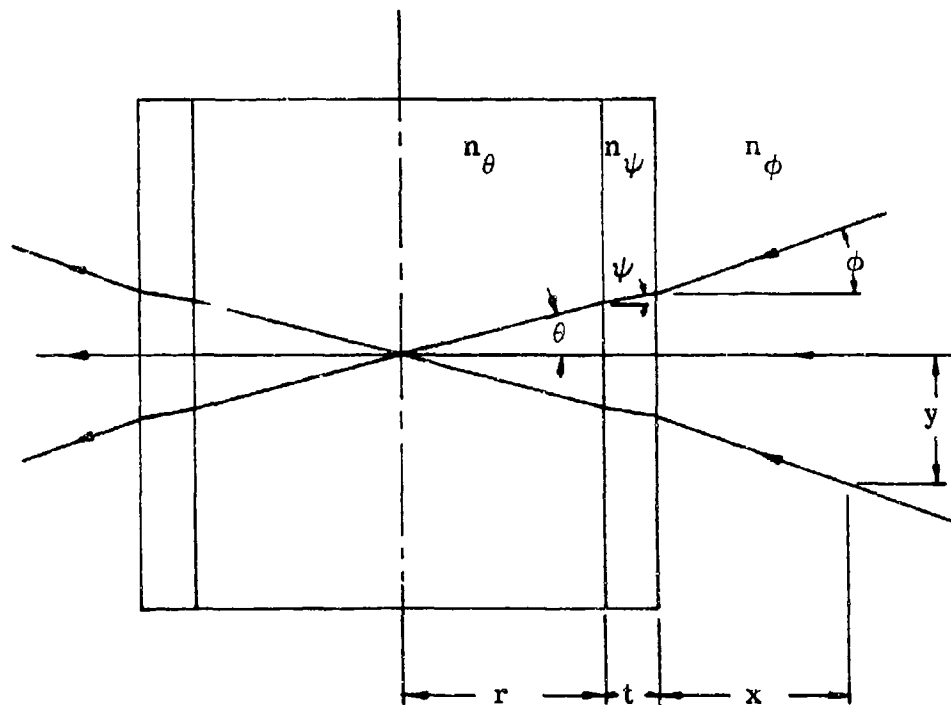


Figure A.1

The Refraction of Beams Due to the Presence of the Test Section and Water

If we note that

$$\lambda_{\theta} = n_{\theta} \lambda$$

$\lambda_{\theta}$ : wavelength of light in the flow

$\lambda$ : wavelength of light in a vacuum

equation (A.1) can be written as

$$(A.5) \quad V_z = \frac{n_{\theta} \lambda (f_{d2} - f_{d1})}{2 \sin \theta} .$$

But in light of equation (A.3) this becomes

$$(A.6) \quad V_z = \frac{n_{\phi} \lambda (f_{d2} - f_{d1})}{2 \sin \phi}$$

or since  $n_{\phi} = 1$

$$(A.7) \quad V_z = \lambda (f_{d2} - f_{d1}) / 2 \sin \phi .$$

Thus the form of equation (A.1) remains the same. The form of equation (A.2) would change, however, if we were to write it in terms of the air variables  $\lambda$  and  $\phi$ .

Let us next consider the following problem: given that the beams are moved an external distance  $dx$  (see Figure A.1), what is the displacement of their intersection  $dr$  ?

Referring to Figure A.1 ,

$$(A.8) \quad y = r \tan \theta + t \tan \psi + x \tan \phi ,$$

$$(A.9) \quad 0 = dr \tan \theta + dx \tan \phi .$$

For small angles

$$(A.10) \quad \tan \theta \approx \sin \theta ,$$

and

$$(A.11) \quad \tan \phi \approx \sin \phi .$$

Therefore

$$(A.12) \quad dr = \frac{-\sin \phi}{\sin \theta} dx .$$

But from equation (A.3)

$$(A.13) \quad dr = \frac{-n}{n_{\theta}} \phi \, dx ,$$

which for our set-up becomes

$$(A.14) \quad dr = \frac{-4}{3} dx .$$

## Appendix B

### MEASUREMENT TECHNIQUE FOR MEASURING THE SWIRL COMPONENT OF VELOCITY

#### 1. Frequency-to-Velocity Relationship

The optical bench used in the present work has the flexibility to allow measurement of the third (swirl) component of velocity. To measure the swirl component, an incident beam,  $\underline{k}_{01}$ , (see Figure B.1) is aligned perpendicular to the flow axis at an angle  $\theta$  with respect to the X axis. Incident beam  $\underline{k}_{02}$ , of equal intensity, (not shown in Figure B.1) is symmetrical to  $\underline{k}_{01}$  about the X axis. The beams intersect at a distance  $\delta$  from the flow axis. Thus, beams  $\underline{k}_{01}$  and  $\underline{k}_{02}$  form a plane perpendicular to the flow axis and are symmetrical about the X axis. Recalling the frequency-to-velocity relationship developed in Chapter 2

$$(B.1) \quad f_d = \frac{f_0}{C} \underline{V} \cdot (\underline{k}_s - \underline{k}_0)$$

where for this beam geometry

$$(B.2) \quad \underline{V} = V_r \underline{e}_r + V_\theta \underline{e}_\theta,$$

$$(B.3) \quad \underline{k}_{01} = \cos \theta \underline{e}_r + \sin \theta \underline{e}_\theta,$$

$$(B.4) \quad \underline{k}_{02} = \cos \theta \underline{e}_r - \sin \theta \underline{e}_\theta,$$

and

$$(B.5) \quad \underline{k}_s = \underline{k}_{s1} = \underline{k}_{s2}.$$



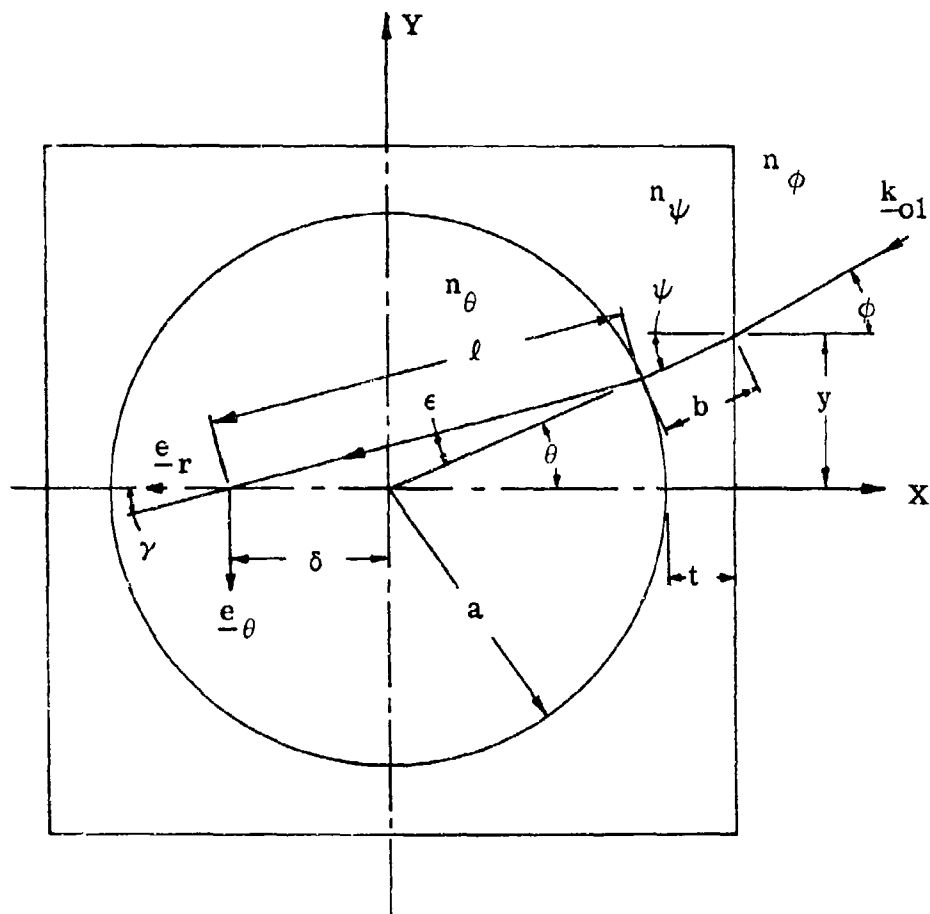


Figure B.1

Top View of the Test Section Showing the Refraction of the Beam  
 Geometry Used to Measure the Swirl Component of Velocity  
 Due to the Presence of the Test Section and Water

This last equation implies that we are sensing (with a P. M.) the scattering due to both  $\underline{k}_{01}$  and  $\underline{k}_{02}$  along the same direction,  $\underline{k}_s$ .

Continuing,

$$(B.6) \quad f_{d1} = \frac{f_0}{C} [-V_r \cos \theta - V_\theta \sin \theta + \underline{V} \cdot \underline{k}_s]$$

and

$$(B.7) \quad f_{d2} = \frac{f_0}{C} [-V_r \cos \theta + V_\theta \sin \theta + \underline{V} \cdot \underline{k}_s] .$$

As seen in Chapter IV, the P. M. tube senses the difference frequency of two beams impinging on its face which, in this case, is  $f_{d2} - f_{d1}$ .

$$(B.8) \quad f_{d2} - f_{d1} = 2 \frac{f_0}{C} V_\theta \sin \theta ,$$

$$(B.9) \quad V_\theta = \frac{C}{f_0} \frac{(f_{d2} - f_{d1})}{2 \sin \theta} .$$

Let us consider this last equation. It tells us that the frequency-to-velocity relation is not a function of scattered beam position and therefore is not a function of P. M. position. As a consequence, there is no aperture broadening. This beam geometry and its advantages were first noted by Mezunder and Wankum (1970) who call it the differential Doppler anemometer.

## 2. Measurement of Turbulent Fluctuations About a Zero Mean

In the pipe flow being studied, the only non-zero mean velocity is in the axial direction. Thus the radial and swirl velocities have only fluctuating components

$$(B.10) \quad V_r(t) = V'_r(t)$$

and

$$(B.11) \quad V_\theta(t) = V'_\theta(t) .$$

However, the bandwidth of the readout unit used in this work is 50 KHZ - 10 MHZ. It will not measure mean velocities or fluctuations about the mean for velocities corresponding to frequencies under 50 KHZ. Therefore, the readout unit cannot measure  $V'_\theta$  using the beam geometry outlined above unless one creates an artificial mean velocity. This can be accomplished by shifting the frequency of one of the incident beams using a rotating radial diffraction grating (Denison and Stevenson, 1970). Using this device one can shift the incident frequency by  $\Delta f_0$ , where

$$(B.12) \quad \Delta f_0 = w/K .$$

where  $w$  is the angular velocity of the radial diffraction grating and  $K$  is a grating constant. Frequency shifts of up to 500 KHZ can be easily effected using this technique.

Let us assume that the frequency of the incident beam of Figure A.2 is shifted by  $\Delta f_1$ . The scattering frequency will be

$$(B.13) \quad f_{s1} = f_0 + \Delta f_1 + \frac{(f_0 + \Delta f_1)}{C} \underline{V} \cdot (\underline{k}_s - \underline{k}_{01}) .$$

The scattered frequency of beam 2, as before, is

$$(B.14) \quad f_{s2} = f_0 + \frac{f_0}{C} \underline{V} \cdot (\underline{k}_s - \underline{k}_{02}) .$$

Note that  $\underline{k}_s = \underline{k}_{s1} = \underline{k}_{s2}$  since a differential Doppler configuration is being used. The P.M. tube sees the difference frequency

$$(B. 15) \quad f_{s1} - f_{s2} = \Delta f_1 + \frac{f_o}{C} \underline{V} \cdot (\underline{k}_{02} - \underline{k}_{01}) + \frac{\Delta f_1}{C} \underline{V} \cdot (\underline{k}_s - \underline{k}_{01}) .$$

If  $f_{s1} - f_{s2}$  is to take on a simple form,

$$(B. 16) \quad \underline{k}_s = \underline{k}_{01} .$$

Therefore

$$(B. 17) \quad f_D = f_{s1} - f_{s2} = \Delta f_1 + \frac{f_o}{C} \underline{V} \cdot (\underline{k}_{02} - \underline{k}_{01}) ,$$

which becomes, referring to Figure A. 2

$$(B. 18) \quad f_D = \Delta f_1 + \frac{2f_o}{C} V' \sin \theta .$$

Thus,  $\Delta f_1$  represents a mean velocity and the second term the frequency fluctuating about  $\Delta f_1$ . Note, however, in simplifying the frequency-velocity relationship the advantage of the differential Doppler has been lost since the position of  $\underline{k}_s$  has been defined.

### 3. Refractive Effect of Test Section and Water on Beam Geometry

In order to measure a velocity profile across the test section, it is necessary to know the relationship between the incremental movement of the optical bench and the resulting incremental motion of the beam intersection (measuring volume) within the test section. This relationship is not simple due to the refraction of the incident beam by the test section.

Assume the initial distance of the incident beam from the reference beam at the front surface of the test section is known to be  $y_i$ . If the optical bench is moved a distance  $\Delta x$  in the negative X direction, the incident beam intersects the test section a distance  $y = y_i + \Delta x \tan \phi$  from the reference beam. Using Snell's law (see Figure B. 1)

$$(B.19) \quad \psi = \arcsin \left( \frac{n}{n_\phi} \sin \phi \right) .$$

Noting that the distance  $(a + t)$  from the center of the test section to its front edge can be written as

$$(B.20) \quad a \cos \theta + b \cos \psi = a + t ,$$

also

$$(B.21) \quad a \sin \theta + b \sin \psi = y .$$

These equations can be combined to yield

$$(B.22) \quad \sin (\theta - \psi) = \frac{(a+t)}{a} \sin \psi - \frac{y}{a} \cos \psi .$$

Again using Snell's law

$$(B.23) \quad \sin \epsilon = \frac{n_\theta}{n_\psi} \sin (\theta - \psi)$$

or

$$(B.24) \quad \sin \epsilon = \frac{n_\theta}{n_\psi} \left[ \frac{(a+t)}{a} \frac{n_\psi}{n_\phi} \sin \phi - \frac{y}{a} \cos \left( \sin^{-1} \left( \frac{n_\psi}{n_\phi} \sin \phi \right) \right) \right] .$$

Now

$$(B.25) \quad \gamma = \theta + \epsilon ,$$

$$(B. 26) \quad l = \frac{a \sin \theta}{\sin \theta + \epsilon} ,$$

and

$$(B. 27) \quad \delta = a \cos \theta - l \cos (\theta + \epsilon) .$$

Equations (B. 22), (B. 24), (B. 26), and (B. 27) can be solved successively to obtain  $\delta$ , the incremental movement of the beam intersection relative to the flow axis.